ATLAS CONF Note

ATLAS-CONF-2021-015

1st April 2021

Search for long-lived charginos based on a disappearing-track signature using 136 fb^{-1} of pp collisions at $\sqrt{s}$ = 13 TeV with the ATLAS detector

The ATLAS Collaboration

A search for long-lived charginos produced either directly or in the cascade decay of heavy prompt gluino states is presented. The search is based on proton-proton collision data collected at a center-of-mass energy of $\sqrt{s}$ = 13 TeV between 2015 and 2018 with the ATLAS detector at the LHC, corresponding to an integrated luminosity of 136 fb^{-1}. Long-lived charginos are characterised by a distinct disappearing track signature and are reconstructed using at least four measurements in the ATLAS pixel detector, with no subsequent measurements in outermost silicon tracking volume nor any associated energy deposits in the calorimeter. The final state is complemented by at least one high transverse momentum jet and large missing transverse momentum for triggering purposes. No excess above the expected backgrounds is observed. Exclusion limits are set at 95% confidence level on the masses of the chargino and gluinos for different chargino lifetimes. Chargino masses up to 660 (210) GeV are excluded in scenarios where the chargino is a pure wino (higgsino). For charginos produced during the cascade decay of a heavy gluino, gluinos with masses up to 2.1 TeV are excluded for a chargino mass of 300 GeV and a variety of chargino lifetimes.

ATLAS-CONF-2021-015
31 March 2021

1 Introduction

Supersymmetry (SUSY) [1–6] is a space-time symmetry that extends the Standard Model (SM), predicting the existence of partners for each SM particle. This extension presents solutions to insufficiencies in the SM, such as providing a candidate for dark matter as the Lightest Supersymmetric Particle (LSP) and a solution to the hierarchy problem. Superpartners of the SM particles have identical quantum numbers to their partner particles but differ by one half unit of spin. Supersymmetric partners of the electroweak gauge bosons and the Higgs bosons, collectively referred to as electroweakinos, consist of the bino, winos, and higgsinos, which mix to form neutral and charged mass eigenstates called neutralinos and charginos respectively. The winos are the superpartners of the SU(2) gauge fields, the bino is the superpartner of the U(1) gauge field, and the higgsinos are the superpartners of the Higgs fields.

Mass differences between the lightest neutralino ($\tilde{\chi}_1^0$) and the lightest chargino ($\tilde{\chi}_1^\pm$), $\Delta m\,(\tilde{\chi}_1^\pm, \tilde{\chi}_1^0)$, are predicted to be of the order of 100 MeV by radiative SM correction [7, 8] in scenarios where the LSP is wino-like and other SUSY particles are decoupled. In particular, Anomaly-Mediated Supersymmetry Breaking (AMSB) models [9, 10] give rise to such differences and naturally predict a pure wino LSP. The mass splitting between the charged and neutral wino in such scenarios is suppressed at tree level by the approximate custodial symmetry; it has been calculated at the two-loop level to be around 160 MeV [7], corresponding to a chargino lifetime of about $\tau_{\tilde{\chi}_1^\pm} = 0.2$ ns.

In addition to the wino LSP scenarios, a number of "natural" models of SUSY [11–13] predict a light higgsino LSP with masses as light as the electroweak scale. In these scenarios, the higgsino mass parameter $|\mu|$ is small compared to the other electroweak gaugino mass scales. At tree level, the charged and neutral states are all mass degenerate, but due to higher order SM loop corrections a mass splitting of approximately 300 MeV is generated. Such a mass splitting gives rise to higgsinos with decay lengths given by [8]:

$$c\tau[\text{mm}] \sim 7 \times \left[\left(\frac{\Delta m\left(\tilde{\chi}_1^\pm, \tilde{\chi}_{1,2}^0\right)}{340\ \text{MeV}}\right)^3 \sqrt{1 - \frac{m_{\pi^\pm}^2}{\Delta m\left(\tilde{\chi}_1^\pm, \tilde{\chi}_{1,2}^0\right)^2}}\right]^{-1},$$

where $m_{\pi^\pm}$ is the mass of the charged pion, $\Delta m\left(\tilde{\chi}_1^\pm, \tilde{\chi}_{1,2}^0\right)$ is the mass difference between the lightest chargino and either of the two lightest mass degenerate neutralinos. For chargino masses ranging from 150 GeV to 1000 GeV, the mass splitting ranges from approximately 280 MeV to 350 MeV leading to charginos with $c\tau \sim 14$ mm ($\tau_{\tilde{\chi}_1^\pm} = 0.048$ ns) to 7 mm ($\tau_{\tilde{\chi}_1^\pm} = 0.026$ ns).

In both the wino and higgsino scenarios, the chargino can be produced with large momentum and live long enough to traverse multiple layers of the ATLAS pixel detector before decaying. It decays primarily to a neutral weakly interacting LSP and a low momentum pion. Before it decays, the chargino deposits energy in the innermost tracking layers that can be reconstructed into a short track if at least four pixel layers have been hit. The weakly interacting LSP will escape detection and lead to missing transverse momentum, while the pion from the chargino decay has too low momentum to be reconstructed as a track, resulting in a characteristic signature where the short track from the chargino disappears. By requiring at least four hits[1] to reconstruct a disappearing track, the higgsino-like scenarios are considerably more challenging than the wino-like models from an experimental perspective due to the extremely short lifetime predicted in the higgsino models.

[1] Hits are defined as measurements in the pixel, SCT or TRT detectors.

This paper targets two production processes, the electroweak production of charginos and neutralinos, and the strong production of gluinos where charginos are produced during the cascade decay of the gluino, as shown in Figure 1. In both scenarios, the chargino is long-lived and reconstructed from energy deposits in the ATLAS pixel detector. For the electroweak production process, a high momentum jet from initial-state-radiation (ISR) is required to ensure significant missing transverse momentum allowing to trigger on the events. The final state selections of the electroweak and strong production channels are characterised by at least one and at least four jets, respectively, large missing transverse momentum, and at least one disappearing track with large transverse momentum.

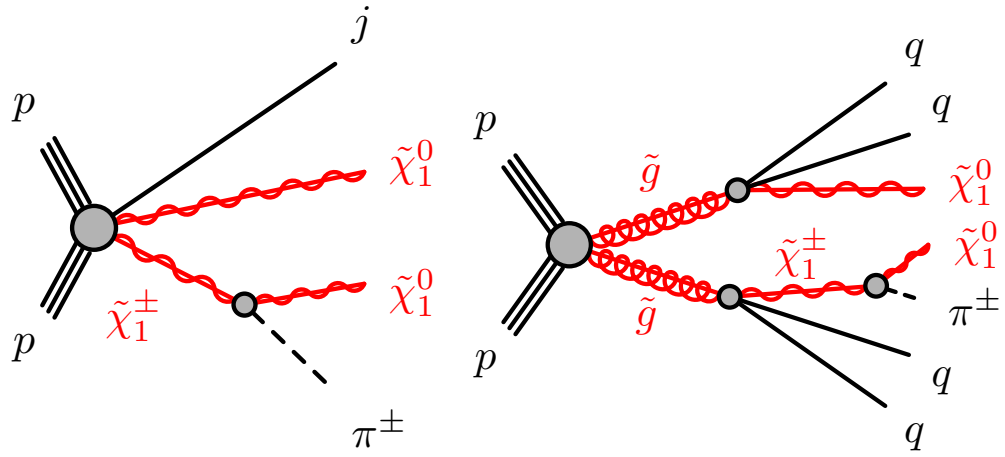

(a) $pp \to \tilde{\chi}_1^\pm \tilde{\chi}_1^0 j$ (b) $pp \to qqqq\tilde{\chi}_1^\pm \tilde{\chi}_1^0$

Figure 1: Example diagrams for the electroweak (a) and strong (b) production channel signal models. The signal signature consists of a long-lived chargino, missing transverse momentum and quarks or gluons, which are observed as jets, and which originate from initial state radiation (a) or in the cascade decay of the gluino (b).

Previous searches for long-lived charginos resulting in a disappearing track signature were performed by ATLAS [14, 15] using 36.1 fb^{-1} of proton-proton collision data at a center-of-mass energy of $\sqrt{s}$ = 13 TeV. The previous ATLAS results benefited from the inclusion of the innermost pixel tracking layer installed at a radius of approximately 33 mm during the LHC long shutdown between Run 1 and Run 2. The extra layer of pixel detector allowed the previous analysis to reconstruct shorter tracks than the Run-1 analysis [16] and to improve sensitivity to shorter chargino lifetimes. The previous ATLAS results excluded pure winos up to chargino masses of 460 GeV and pure higgsinos up to chargino masses of 152 GeV. For the production of gluinos, gluino masses were excluded up to 1.64 TeV for an assumed chargino mass of 460 GeV and 0.2 ns lifetime. The CMS Collaboration has searched for long-lived charginos [17] using 101 fb^{-1} of data at a center-of-mass energy of $\sqrt{s}$ = 13 TeV, excluding charginos in the wino-like models for masses below 884 (474) GeV for a lifetime of 3 (0.2) ns.

In this paper, the sensitivity to charginos with natural wino and higgsino lifetimes is significantly improved due to the increase in the dataset luminosity and additional track quality criteria that enhance the rejection of dominant backgrounds.

The paper is structured as follows. A brief overview of the ATLAS detector is given in Section 2. Section 3 provides details about the data samples, trigger, and simulated signal processes used in this analysis. The reconstruction algorithms and event selection are presented in Sections 4 and 5 respectively. Backgrounds

are estimated in a fully data-driven manner and described in Section 6. The systematic uncertainties are described in Section 7. The observed events in the signal and validation regions, and the statistical interpretation of the results are presented in Section 8. Section 9 is devoted to the conclusions.

2 ATLAS Detector

ATLAS [18] is a multipurpose detector with a forward-backward symmetric cylindrical geometry, covering nearly the entire solid angle around an interaction point of the LHC[2]. The inner tracking detector (ID) consists of pixel and micro-strip silicon detectors covering the pseudorapidity region of $|\eta| < 2.5$, surrounded by a transition radiation tracker (TRT), which improves the momentum measurement and enhances electron identification capabilities. The pixel detector spans the radius range from 3 cm to 12 cm, the strip semiconductor tracker (SCT) from 30 cm to 52 cm, and the TRT from 56 cm to 108 cm. The pixel detector has four barrel layers, and three disks in each of the forward and backward regions. The barrel layers surround the beam pipe at radii of 33.3, 50.5, 88.5, and 122.5 mm, covering $|\eta| < 1.9$. These layers are equipped with pixels which have a width of 50 μm in the transverse direction. The pixel sizes in the longitudinal direction are 250 μm for the first layer and 400 μm for the other layers. The innermost layer, the insertable B-layer [19], was added during the long shutdown between Run 1 and Run 2 and improves the reconstruction of tracklets by adding an additional measurement close to the interaction point. The ID is surrounded by a thin superconducting solenoid providing an axial 2 T magnetic field and by a fine-granularity lead/liquid-argon (LAr) electromagnetic calorimeter covering $|\eta| < 3.2$. The calorimeters in the region of $3.1 < |\eta| < 4.9$ are made of LAr active layers with either copper or tungsten as the absorber material. A steel/scintillator-tile calorimeter provides coverage for hadronic showers in the central pseudorapidity range of $|\eta| < 1.7$. LAr hadronic end-cap calorimeters, which use copper as an absorber, cover the forward region of $1.5 < |\eta| < 3.2$. The muon spectrometer with an air-core toroid magnet system surrounds the calorimeters. The ATLAS trigger system [20] consists of a hardware-based level-1 trigger followed by a software-based high-level trigger.

3 Dataset and Simulated Event Samples

The dataset for this search was collected during Run 2 of the LHC between 2015 and 2018 by the ATLAS experiment at a centre-of-mass energy of $\sqrt{s} = 13$ TeV. The LHC collided protons at bunch-crossing intervals of 25 ns, with the average number of interactions per bunch crossing, μ, ranging between 30 to 70 during the entire data taking period.

Events are required to have been taken during stable beam conditions and when all the detector subsystems were operational. In addition, luminosity blocks, defined to be periods of stable data taking conditions typically 60 seconds long, that have been identified to contain inactive SCT elements due to a power-supply crate trip, module desynchronization, or readout issues are vetoed. This data quality requirement is intended

[2] ATLAS uses a right-handed coordinate system with its origin at the nominal interaction point in the centre of the detector. The positive x-axis is defined by the direction from the interaction point to the centre of the LHC ring, with the positive y-axis pointing upwards, while the beam direction defines the z-axis. Cylindrical coordinates (r, ϕ) are used in the transverse plane, ϕ being the azimuthal angle around the z-axis. The pseudorapidity η is defined in terms of the polar angle θ by $\eta = -\ln\tan(\theta/2)$ and the rapidity is defined as $y = (1/2)\ln[(E + p_z)/(E - p_z)]$ where E is the energy and p_z the longitudinal momentum of the object of interest.

to protect against fake disappearing tracks arising from readout issues in the SCT detector, and results in 2.7 fb^{-1} of data loss.

After the application of additional requirements for beam and detector conditions, inactive SCT element veto, and general data-quality requirements [21], the total integrated luminosity is 136 fb^{-1}. The uncertainty in the combined 2015–2018 integrated luminosity is 1.7 % [22], obtained using the LUCID-2 detector [23] for the primary luminosity measurements.

Events were collected using either missing transverse momentum ($E_{\text{T}}^{\text{miss}}$) or single lepton triggers. The selection thresholds of the $E_{\text{T}}^{\text{miss}}$ triggers varied between 70 GeV to 110 GeV depending on the data taking periods [24], while the single lepton triggers required a single electron or muon with varying thresholds on the transverse momentum and isolation of lepton [25, 26]. The $E_{\text{T}}^{\text{miss}}$ triggers are the main triggers for the signal, control, and validation regions, while the single lepton triggers are used for measurements of the $E_{\text{T}}^{\text{miss}}$ trigger efficiency, transfer factors and smearing functions.

All backgrounds are determined in a data-driven manner. Samples of simulated Monte Carlo (MC) events were used to estimate the experimental sensitivity to possible SUSY models. The SUSY mass spectrum, branching ratios, and decay widths are calculated using ISASUGRA v7.80 [27]. The wino-like models were generated in the minimal AMSB model [9, 10] with $\tan\beta = 5$ and with a positive sign of the higgsino mass parameter. The signal MC samples are generated using MadGraph5 v2.6.2 [28] with up to two additional partons at leading-order in the matrix-element, and interfaced to Pythia8 v8.230 [29] and EvtGen v.1.6.0 [30] for parton showering and hadronisation. The CKKW-L merging scheme [31] was applied to combine the matrix elements with the parton shower. The A14 tune [32] of Pythia8 is used with the NNPDF2.3LO parton distribution function (PDF) set. A detector simulation based on Geant4 [33, 34] is used to simulate the passage of particles through the ATLAS detector. For electroweak production, production modes of $\tilde{\chi}_1^{\pm}\tilde{\chi}_1^{\pm}$, $\tilde{\chi}_1^0\tilde{\chi}_1^{\pm}$ (and $\tilde{\chi}_1^{\pm}\tilde{\chi}_2^0$) are considered for wino (higgsino) models. For the chargino decay in the higgsino model, branching ratios of 95.5% for $\tilde{\chi}_1^{\pm} \to \pi^{\pm}\tilde{\chi}_1^0$, 3% for $\tilde{\chi}_1^{\pm} \to e^{\pm}\nu\tilde{\chi}_1^0$ and 1.5% for $\tilde{\chi}_1^{\pm} \to \mu^{\pm}\nu\tilde{\chi}_1^0$ are used [35], while the AMSB model used a 100% branching ratio for $\tilde{\chi}_1^{\pm} \to \pi^{\pm}\tilde{\chi}_1^0$. For the strong production, a simplified model is used assuming branching ratios of the gluino decay are 1/3 for each of $\tilde{g} \to qq\tilde{\chi}_1^0$, $\tilde{g} \to qq\tilde{\chi}_1^-$ and $\tilde{g} \to qq\tilde{\chi}_1^+$. Only four flavours of quarks are considered for the strong production model: d, u, c and s.

The cross-sections for the electroweak and strong production models are calculated at next-to-leading order (NLO) in the strong coupling constant using Prospino2 [36]. The higgsino cross sections are approximately a factor of 4 smaller than the AMSB wino-like models for the electroweak production. The strong production includes resummation of soft-gluon emissions at next-to-leading-logarithm accuracy. Uncertainties from variations of the renormalization and factorization scales are included by varying the scales by a factor of two or one half of their nominal values.

Inelastic pp interactions were generated using Pythia8 v8.186 and EvtGen v.1.6.0 with the NNPDF2.3LO PDF set. The inelastic collisions were overlaid onto the hard-scattering process to simulate the effect of multiple pp interactions. MC samples were reweighted to match the distribution of the average number of interactions per bunch crossing observed in data.

4 Object Reconstruction

Primary vertices are reconstructed from at least two tracks with transverse momentum $p_{\mathrm{T}} > 500$ MeV. All vertices within the beam spot area are considered as primary vertices. The vertex with the largest sum p_{T}^2 of associated tracks is defined to be the hard-scattering vertex. Events are required to have at least one hard-scatter vertex to be considered for analysis.

Electron candidates are reconstructed using energy clusters in the electromagnetic calorimeter which are matched to an inner detector track [37]. They are required to have $p_{\mathrm{T}} > 10$ GeV and $|\eta| < 2.47$, and must satisfy the "LooseAndBLayerLLH" quality criteria [38]. In order to ensure that the trajectories of the electrons are consistent with originating from the hard-scatter vertex, the longitudinal impact parameter measured relative to the hard-scatter vertex (z_0^{HS}) must satisfy $|z_0^{\mathrm{HS}} \sin\theta| < 0.5$ mm, and the transverse impact parameter significance (d_0/σ_{d_0}) must be less than 5. Electrons are required to be isolated from other objects by using a combination of track and calorimeter based information. The sum of the transverse energy within a cone $\Delta R = \sqrt{(\Delta\eta)^2 + (\Delta\phi)^2} < 0.4$ around the electron candidate, divided by the electron's transverse energy, is required to be less than 0.15 (0.20) for track (calorimeter) based isolation criteria.

Muons are reconstructed from a combination of inner detector and muon spectrometer (MS) tracks [39]. They are required to satisfy the 'Medium' quality requirements described in Ref. [39] and have $p_{\mathrm{T}} > 10$ GeV and $|\eta| < 2.7$. Muons tracks are required to originate from the hard-scatter vertex of the event by applying $|z_0^{\mathrm{HS}} \sin\theta| < 0.5$ mm and $d_0/\sigma_{d_0} < 3$. The muons are required to be isolated, using the same requirements as those used for electrons. Muons, reconstructed using only information in the muon spectrometer are used to estimate muon backgrounds as described in Section 6.2, and are referred to as standalone muons. No constraint is placed on the interaction region during the reconstruction of standalone muons.

Jet candidates are reconstructed from three-dimensional topological energy clusters [40] using the anti-k_t algorithm [41, 42] with radius parameter $R = 0.4$. Jets are corrected to particle level by the application of a jet energy scale (JES) calibration derived from simulation and by *in-situ* corrections obtained from 13 TeV data [43]. Jets are required to have $p_{\mathrm{T}} > 20$ GeV and $|\eta| < 2.8$. In order to reduce contributions from pile-up jets, all jets with $|\eta| < 2.5$ and $p_{\mathrm{T}} < 60$ GeV are required to satisfy the jet-to-vertex tagger (JVT) [44] requirements. The tagger is configured to have a 92% efficiency to identify jets from the hard-scatter vertex.

An overlap removal is performed for all objects to avoid double counting. If an electron and a jet are separated by $\Delta R < 0.2$, the electron candidate is kept and the jet is discarded. For jets surviving this requirement, if an electron or muon is separated by $\Delta R < 0.4$ to the jet, the jet is kept and the electron or muon is discarded.

The missing transverse momentum is reconstructed as the negative vector sum of the transverse momentum of photons, electrons, muons and jets, and a soft-term. The soft-term is reconstructed from tracks that have been associated with the hard-scatter vertex but do not overlap with any object already counted [45, 46].

Tracks are reconstructed from a combination of at least seven hits in the pixel and SCT detector system [47, 48]. The majority of charginos decay before passing through enough detector layers to satisfy the minimum number of silicon hit requirements for track reconstruction. A second-pass track reconstruction is performed where hits used by the primary track reconstruction are masked to avoid efficiency deterioration due to accidentally mis-reconstructed tracks using hits which do not originate from charginos. The second-pass track reconstruction is seeded by four hits in the innermost pixel system only, and the tracks are extended

into the SCT and TRT detectors. Such tracks are referred to as *pixel tracklets*, and are reconstructed from at least four hits in the ATLAS pixel detector.

Pixel tracklets are required to pass a series of quality and selection criteria in order to reject fake tracklets. The selection of pixel tracklets has been developed specifically for this search and is optimised to maintain high signal selection efficiency and good background rejection. In addition to the requirement of four pixel hits on unique pixel layers, the pixel tracklet must have a pixel hit on the innermost pixel layer, must not have any hits that deviate significantly from the tracklets trajectory, and all four pixel hits must exist on consecutive pixel layers.

The chi-squared probability for each tracklet, which is calculated from fit result locations and the measured hit locations, must be greater than 0.1. The transverse momentum and the pseudorapidity of the tracklet should satisfy $p_{\mathrm{T}} > 20$ GeV and $0.1 < |\eta| < 1.9$. Impact parameter requirements are applied to the pixel tracklets to ensure that they originate from the hard-scatter interaction. The requirements are $|d_0/\sigma_{d_0}| < 1.5$ and $|z_0^{\mathrm{HS}} \sin\theta| < 0.5$ mm.

Finally, the tracklet is required to be isolated from other tracks in the event: the sum of track momenta within $\Delta R < 0.4$ from the pixel tracklet, relative to the tracklet momentum is required to be less than 4%. An overlap removal is applied for the tracklet: if an electron or a MS track are separated by $\Delta R < 0.4$, the tracklet candidate is discarded.

The pixel tracklets for the signal events are characterised by a lack of hits in the outermost silicon trackers and no calorimeter activity. Together these two requirements define the *disappearing track* condition. The first condition is enforced by a veto on any SCT hits. The second condition is a newly developed selection criterion with regard to the previous ATLAS results [14, 15]. Since electron and hadron backgrounds tend to deposit significant energy into the calorimeters, limiting the calorimeter energy along the trajectory of the pixel tracklet has a strong impact in separating signal from the electron and hadron backgrounds.

The calorimeter energy $E_{\mathrm{T}}^{\text{topo cluster}}$ is calculated from the sum of topological energy clusters in the calorimeter whose angular separation with the pixel tracklet is $\Delta R < 0.2$. The pointing resolution in both η and ϕ of the pixel tracklets is found to be better than 0.1 in all regions of the detector. An upper requirement of $E_{\mathrm{T}}^{\text{topo cluster}} < 5$ GeV is applied to all pixel tracklets. Figure 2 shows a comparison of calorimeter energy between simulated signal and data-driven background predictions obtained as described in Section 6.

5 Signal Region Selection

Signal events for this analysis are characterised by a distinctive signature composed of a disappearing track and large missing transverse momentum. The disappearing track criteria are implemented through a veto on any SCT hits, and a lack of significant energy in the calorimeter as described in the previous section. Signal regions are designed to separately target the electroweak and strong production models shown in Figure 1.

A common preselection is applied to all events selected for the signal regions. Events are required to contain at least one high momentum jet with $p_{\mathrm{T}} > 100$ GeV and satisfy the $E_{\mathrm{T}}^{\mathrm{miss}}$ trigger requirements described in Section 3. For events containing multiple pixel tracklets satisfying all of the quality criteria described in Section 4, the one with the highest transverse momentum is chosen. In order to reduce contributions from background events such as top-pair and W/Z + jets production, events are vetoed if they contain any electron or muon candidates.

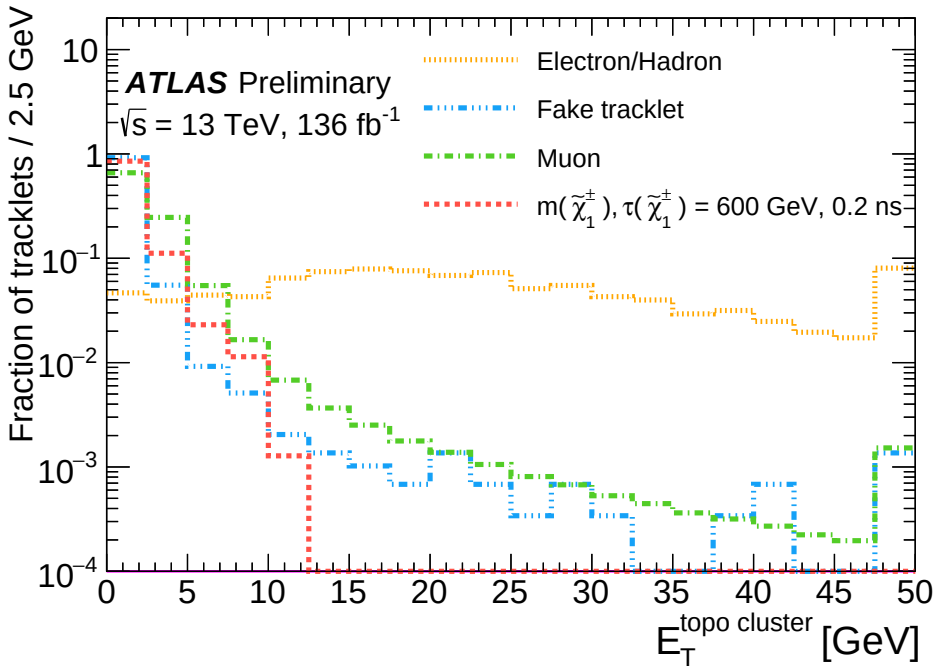

Figure 2: Distribution of calorimeter energy found within $\Delta R < 0.2$ of the pixel tracklet for a simulated signal prediction with $m_{\tilde{\chi}_1^\pm} = 600$ GeV and $\tau_{\tilde{\chi}_1^\pm} = 0.2$ ns. Background processes arising from scattering electrons, hadrons and muons, and combinational fake tracks, are also shown. Background predictions are obtained from data; the electron and hadron components are derived from events with tracklet $p_{\mathrm{T}} < 60$ GeV and $E_{\mathrm{T}}^{\mathrm{miss}} > 100$ GeV, as the electron and hadron control regions, defined in Section 6, include a requirement on $E_{\mathrm{T}}^{\mathrm{topocluster}}$. All predictions have been normalised to unity. The last bin includes entries from the overflow bins.

In this analysis, the $E_{\mathrm{T}}^{\mathrm{miss}}$ trigger efficiency is measured in data and used instead of the simulated trigger. In order to evaluate the $E_{\mathrm{T}}^{\mathrm{miss}}$ trigger efficiency for signal-like events, a data control sample consisting of events with exactly one muon matched to the single muon trigger with $p_{\mathrm{T}} > 27$ GeV is used. Since muon candidates are not included as visible objects in the hardware-based Level-1 $E_{\mathrm{T}}^{\mathrm{miss}}$ trigger, $W \to \mu\nu$ events have a similar signature to signal events and can be used to quantify the trigger performance. In order to select events consistent with a $W \to \mu\nu$ decay, events are required to have 30 GeV $< m_{\mathrm{T}} <$ 100 GeV, where m_{T} is defined by:

$$m_{\mathrm{T}} = \sqrt{2 p_{\mathrm{T}}^{\mu} E_{\mathrm{T}}^{\mathrm{miss}} \left[1 - \cos\Delta\phi(\mu, E_{\mathrm{T}}^{\mathrm{miss}})\right]}.$$

The $E_{\mathrm{T}}^{\mathrm{miss}}$ trigger efficiency is calculated as the fraction of these events passing the $E_{\mathrm{T}}^{\mathrm{miss}}$ trigger to the total number of events.

The efficiencies depend on the trigger thresholds used during a given data-taking period, and reach a plateau between $E_{\mathrm{T}}^{\mathrm{miss}}$ values from 50 GeV to 200 GeV. Above 200 GeV, the trigger efficiency is nearly 100%. For selections with $E_{\mathrm{T}}^{\mathrm{miss}}$ below 200 GeV, such as the control and validation regions described in Section 6.1, the event selection efficiency is significantly impacted by the trigger efficiency turn-on. In order to factor out differences in the efficiencies between data and simulation, all simulated signal predictions apply the

efficiencies from the data efficiency measurement. The efficiencies are determined in equidistant bins of $E_{\mathrm{T}}^{\mathrm{miss}}$ with a width of 10 GeV.

Events are separated into two signal regions to target the electroweak and strong production modes[3]. For the signal regions targeting the electroweak (strong) production, the offline $E_{\mathrm{T}}^{\mathrm{miss}}$[4] is required to be greater than 200 (250) GeV. A higher $E_{\mathrm{T}}^{\mathrm{miss}}$ requirement is found to be optimal for the strong production channel due to the large Lorentz boost of the neutralinos produced during the decay of a heavy gluino particle. Additionally, the strong production signal region requires at least three jets with p_{T}> 20 GeV. In order to reduce contributions from processes that generate fake instrumental $E_{\mathrm{T}}^{\mathrm{miss}}$ due to potential jet mis-measurements, the azimuthal distance $\Delta\phi_{min}^{\mathrm{jet}-E_{\mathrm{T}}^{\mathrm{miss}}}$, which is defined by taking the ϕ direction difference between the missing transverse momentum and each of the four highest p_{T} jets with $p_{\mathrm{T}} > 50$ GeV, is required to be greater than 1.0 (0.4) for the electroweak (strong) production signal regions. The signal region selection criteria are summarized in Table 1.

The full transverse momentum distribution of the selected pixel tracklets is fitted to estimate the backgrounds and sensitivity to the signals. Since the signal is characterised by a high momentum chargino, the majority of the signal events contain a high transverse momentum pixel tracklet. For the model-independent interpretation of the results, the pixel tracklet is required to have $p_{\mathrm{T}} > 60$ GeV as shown in Section 8.

Signal region	Electroweak production	Strong production
Number of electrons and muons	0	
Number of pixel tracklets	≥ 1	
$E_{\mathrm{T}}^{\mathrm{miss}}$ [GeV]	> 200	> 250
Number of jets (p_{T}> 20 GeV)	≥ 1	≥ 3
Leading jet p_{T} [GeV]	> 100	> 100
Second and third jet p_{T} [GeV]	–	> 20
$\Delta\phi_{min}^{\mathrm{jet}-E_{\mathrm{T}}^{\mathrm{miss}}}$	> 1.0	> 0.4

Table 1: Signal region selection for electroweak and strong production channels. Entries with "–" indicate that no requirement has been placed on the variable.

Table 2 shows the number of expected signal events, normalised to 136 fb^{-1}, satisfying the selections of the electroweak and strong production channels. The electroweak and strong production signals assume $m_{\tilde{\chi}_1^\pm} = 600$ GeV and $(m_{\tilde{g}}, m_{\tilde{\chi}_1^\pm}) = (1.4, 1.1)$ TeV respectively. Unless otherwise indicated, the wino LSP model is assumed for the benchmark signal points. The dominant inefficiency in the pixel tracklet selection arises from the requirement that the tracklet can be reconstructed, and thus have propagated at least to the fourth pixel layer at a radius of 122.5 mm. Such a requirement implies that charginos have a significant Lorentz boost.

[3] The two signal regions are not orthogonal.

[4] The offline $E_{\mathrm{T}}^{\mathrm{miss}}$ is defined as a missing transverse momentum reconstructed from physics objects which are used in the analysis, the online $E_{\mathrm{T}}^{\mathrm{miss}}$ is a missing transverse momentum at the trigger level.

Signal production channel	Electroweak production		Strong production	
$\tau_{\tilde{\chi}_1^\pm}$	0.2 ns	1.0 ns	0.2 ns	1.0 ns
$E_{\mathrm{T}}^{\mathrm{miss}}$ trigger	770.8 ± 6.8	775.3 ± 5.2	3177 ± 22	3177 ± 22
Lepton veto	769.4 ± 6.8	774.2 ± 5.2	3165 ± 22	3165 ± 22
$E_{\mathrm{T}}^{\mathrm{miss}} > 200$ GeV	394.5 ± 5.2	390.9 ± 4.0	–	–
$E_{\mathrm{T}}^{\mathrm{miss}} > 250$ GeV	–	–	1852 ± 17	1852 ± 17
Leading jet $p_{\mathrm{T}} > 100$ GeV	389.7 ± 5.2	384.9 ± 4.0	1848 ± 17	1848 ± 17
Third jet $p_{\mathrm{T}} > 20$ GeV	–	–	1834 ± 17	1834 ± 17
$\Delta\phi_{\mathrm{min}}^{\mathrm{jet-E_T^{miss}}} > 0.4$	366.7 ± 5.0	362.3 ± 3.9	–	–
$\Delta\phi_{\mathrm{min}}^{\mathrm{jet-E_T^{miss}}} > 1.0$	–	–	1578 ± 16	1578 ± 16
Pixel tracklet selection ($p_{\mathrm{T}} > 60$ GeV)	8.6 ± 0.6	27.3 ± 0.8	16.0 ± 1.3	105.0 ± 3.3

Table 2: Number of expected signal events after each of the selection requirements listed in the Section 5 for the electroweak and the strong production channels as well as for two different chargino lifetimes. Signal predictions are normalised to an integrated luminosity of 136 fb^{-1}. Errors are statistical only.

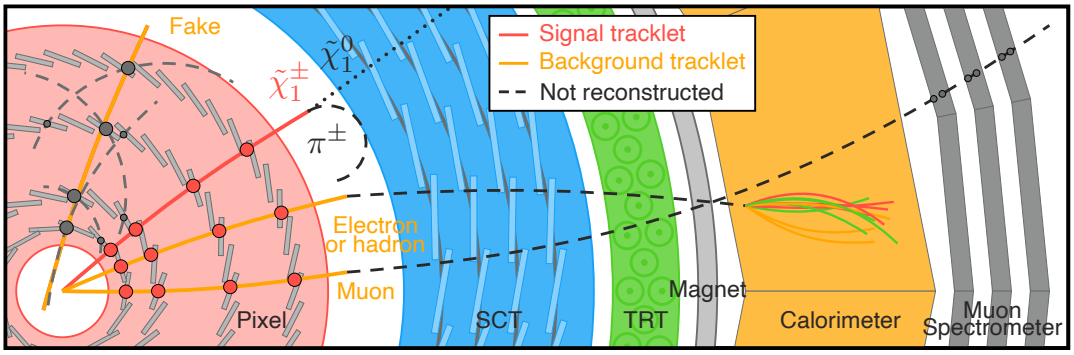

Figure 3: A pictorial representation of signal and background processes. Detectors are not to scale and for illustration purposes only. The signal chargino ($\tilde{\chi}_1^\pm$) decays into a charged pion ($\pi^\pm$) and neutralino ($\tilde{\chi}_1^0$). "Fake", "Muon" and "Electron or hadron" in the figure represent the fake-tracklet background, the muon background and electron or hadron backgrounds respectively.

6 Background Estimation

Backgrounds arise from several sources, and can be separated into two general categories: *charged particle scattering* and *combinatorial fake* backgrounds. All backgrounds are estimated in a fully data-driven manner using an unbinned likelihood fit of background templates to the pixel tracklet p_{T} spectrum. A schematic representation of the various background processes contributing to this analysis, as well as the expected signal signature, is shown in Figure 3.

The scattering of charged particles arises when a lepton changes its direction while propagating through the detector through interaction with the material or bremsstrahlung, and therefore its reconstructed track does not have any associated hits in the SCT and TRT detectors. The dominant underlying processes contributing to the lepton scattering backgrounds are $W \to \ell\nu$ and $t\bar{t}$ production. Contributions from electrons, muons and charged hadrons are estimated separately. The latter includes all physics processes that generate an hadronic final state, such as jets originating from the hadronisation of quarks and gluons. Transfer factors measured in $Z \to \ell\ell$ events and applied to the electron, muon and hadron control regions are used to estimate the templates of the scattering charged particle backgrounds. In the control regions, a lepton or inner detector track is used as a proxy for the pixel tracklet, and its momentum is smeared to match the pixel tracklet transverse momentum.

Combinatorial fake backgrounds arise from combinations of pixel hits from unassociated origins that are in close proximity and reconstructed into a pixel tracklet. The shape of the fake background is estimated using the fake enriched high d_0 control regions described in Section 6.1. The relative contributions of the charged particle scattering and combinational fake backgrounds are constrained in a combined fit as described in Section 6.5.

6.1 Control and validation regions

In order to estimate scattering backgrounds, low-$E_{\mathrm{T}}^{\mathrm{miss}}$, middle-$E_{\mathrm{T}}^{\mathrm{miss}}$, and high-$E_{\mathrm{T}}^{\mathrm{miss}}$ lepton scattering control regions (CRs) are defined. Events selected for the CRs are required to satisfy the $E_{\mathrm{T}}^{\mathrm{miss}}$ trigger requirements and to pass all kinematic selections of the signal regions except the pixel tracklet requirement. The pixel tracklet selection is however replaced with a well identified electron, muon or inner detector track, in order to estimate contributions from electron, muon or hadronic scattering backgrounds, respectively. The leading electron or muon are excluded from the calculation of the missing transverse momentum, in order to reproduce the treatment of the pixel tracklets when calculating the offline $E_{\mathrm{T}}^{\mathrm{miss}}$. Energy deposited by electrons in the calorimeters may be included in the $E_{\mathrm{T}}^{\mathrm{miss}}$ calculation as other objects in the event, but is treated in a similar manner for events with pixel tracklets or when electrons are excluded from the offline $E_{\mathrm{T}}^{\mathrm{miss}}$ calculation. The low and middle $E_{\mathrm{T}}^{\mathrm{miss}}$ requirements are 100 GeV $< E_{\mathrm{T}}^{\mathrm{miss}} <$ 150 GeV and 150 GeV $< E_{\mathrm{T}}^{\mathrm{miss}} <$ 200 GeV, respectively. The high-$E_{\mathrm{T}}^{\mathrm{miss}}$ requirements are the same as for the signal region for which the backgrounds are being estimated: $E_{\mathrm{T}}^{\mathrm{miss}} >$ 200 GeV and $E_{\mathrm{T}}^{\mathrm{miss}} >$ 250 GeV for the electroweak and strong production signal regions, respectively. Events in the lepton scattering CRs are used to calculate the number of pixel tracklets from scattering processes as described in Section 6.2.

A control sample of pure fake pixel tracklets is obtained by applying the same kinematic selection requirements as in the signal regions, but with an inverted cut on the transverse impact parameter of $|d_0/\sigma_{d_0}| > 10$. Events selected for the fake CR are required to satisfy the $E_{\mathrm{T}}^{\mathrm{miss}}$ trigger requirements, but no offline $E_{\mathrm{T}}^{\mathrm{miss}}$ selection is required to increase statistics. Events in the fake control region are used to estimate the shape and number of fake pixel tracklet events in the signal regions as described in the Section 6.4.

A low-$E_{\mathrm{T}}^{\mathrm{miss}}$ pixel-tracklet control region is used in the simultaneous fit described in Section 6.5. This control region has the same selection as the signal region, except for the $E_{\mathrm{T}}^{\mathrm{miss}}$ requirement. Validation Regions (VR) in the middle-$E_{\mathrm{T}}^{\mathrm{miss}}$ selection are used to confirm the modelling of the fit results. A low p_{T} pixel tracklet selection is used to validate the background predictions. In the low p_{T} VR, the pixel tracklet is required to have $p_{\mathrm{T}} <$ 60 GeV in order to reduce the signal contamination at high transverse momentum. In order to validate the fit results across the entire p_{T} spectrum in a low signal contamination region, a middle $E_{\mathrm{T}}^{\mathrm{miss}}$ calorimeter side-band validation region is used. The calorimeter side-band selection requires the pixel tracklet to have 5 GeV$< E_{\mathrm{T}}^{\mathrm{topocluster}} <$ 10 GeV. The signal contamination is less than 10% of the background yield in all control and validation regions.

A summary of the control and validation regions is shown in Table 3.

6.2 Charged-particle background templates

Backgrounds arising from charged particles are estimated using a fully data-driven method. Transfer factors are derived using a $Z \rightarrow \ell\ell$ tag-and-probe method. In this method, a good quality tag electron or muon with $p_{\mathrm{T}} >$30 GeV that is matched to any of the single lepton triggers described in Section 3 is selected for analysis. Probe leptons are identified via either a calorimeter cluster, a muon track reconstructed in the MS detector only, or a high quality inner detector track, depending on the measurement as described below. Transfer factors are defined that assess the probability that a lepton is mis-identified as a pixel tracklet and fulfils the full set of pixel tracklet selection criteria, and are used to scale the events in the electron or muon control regions defined in Table 3 to obtain an estimate for the number of events from charged particle scattering in the signal regions.

Region	$E_{\mathrm{T}}^{\mathrm{miss}}$ condition	Track condition
Control regions		
Electron	e-subtracted $E_{\mathrm{T}}^{\mathrm{miss}}$	well-identified electron
Muon	μ-subtracted $E_{\mathrm{T}}^{\mathrm{miss}}$	well-identified muon
Hadron	standard $E_{\mathrm{T}}^{\mathrm{miss}}$	inner detector track
Fake-tracklet	standard $E_{\mathrm{T}}^{\mathrm{miss}}$	pixel tracklet with $\lvert d_0/\sigma_{d_0}\rvert > 10$
Low-$E_{\mathrm{T}}^{\mathrm{miss}}$ control region		
Low-$E_{\mathrm{T}}^{\mathrm{miss}}$	standard $E_{\mathrm{T}}^{\mathrm{miss}}$	pixel tracklet
Middle-$E_{\mathrm{T}}^{\mathrm{miss}}$ validation regions		
Low p_{T}	standard $E_{\mathrm{T}}^{\mathrm{miss}}$	pixel tracklet with $p_{\mathrm{T}} < 60$ GeV
Calorimeter side-band	standard $E_{\mathrm{T}}^{\mathrm{miss}}$	pixel tracklet with 5 GeV$< E_{\mathrm{T}}^{\mathrm{topocluster}} < 10$ GeV

Table 3: A summary of control and validation regions definitions. The track condition corresponds to the modified selection on the pixel tracklet, or tracks used as a proxy to the pixel tracklet to estimate background processes. The table shows the treatment of the $E_{\mathrm{T}}^{\mathrm{miss}}$ for the lepton scattering backgrounds. The electron, muon and hadron control regions are defined for each of the low, middle and high $E_{\mathrm{T}}^{\mathrm{miss}}$ selections as described in the text.

All probe leptons are required to have p_{T} >10 GeV and $|\eta| < 2.5$. In order to select events originating from $Z \to \ell^{\pm}\ell^{\mp}$ decays, the probe lepton is required to have opposite charge to the tag-lepton, and the invariant mass of the tag-and-probe pair is required to have 81 GeV$< m_{\mathrm{tag,probe}} <$ 101 GeV. Backgrounds to this measurement are estimated by subtracting same-sign tag-probe pairs from the opposite-sign selection.

The templates for the shape of electron scattering backgrounds are estimated by multiplying the number of events in the single-electron control region with a set of transfer factors. The electron transfer factors are factorized into two components: pixel tracklet and calorimeter isolation selections, and the final estimate is given by ,

$$f_{SR}^{e}(p_{\mathrm{T}},\eta) = N_{e,\mathrm{signal}}^{\mathrm{CR}}(p_{\mathrm{T}},\eta) \times \mathrm{TF}_{\mathrm{pixel-only}}^{e}(p_{\mathrm{T}},\eta) \times \mathrm{TF}_{\mathrm{calo-veto}}^{e}(p_{\mathrm{T}},\eta), \quad (1)$$

where $N_{e,\mathrm{signal}}^{\mathrm{CR}}$ is the number of events in the single-electron CR, $\mathrm{TF}_{\mathrm{pixel-only}}^{e}$ is a transfer factor for an electron failing to satisfy the electron identification and being instead mistakenly categorized as a pixel tracklet, and $\mathrm{TF}_{\mathrm{calo-veto}}^{e}$ is the transfer factor assessing the probability for an electron track to be isolated from a calorimeter cluster.

In the pixel tracklet transfer factor measurement, the probe lepton is a calorimeter cluster, and the transfer factor $\mathrm{TF}_{\mathrm{pixel-only}}^{e}$ is calculated as the ratio of the number of probes matched to a pixel tracklet to the number of probes matched to an electron. An object is considered matched if $\Delta R(\mathrm{probe},\mathrm{object}) < 0.2$. Both the pixel tracklet and the track associated to the electron must pass the requirements for the pixel tracklet defined in Section 4, without applying the disappearing track condition for the electron. The calorimeter isolation transfer factor $\mathrm{TF}_{\mathrm{calo-veto}}^{e}$ is calculated using a high quality inner detector track as the probe. The inner detector track is required to pass the same quality criteria as the pixel tracklets, except that instead of the disappearing track condition, the track is required to have at least 8 SCT hits. This measurement assesses the fraction of inner detector tracks passing the calorimeter isolation requirement,

$E_{\mathrm{T}}^{\text{topo cluster}} < 5$ GeV, over the number failing this requirement. Both transfer factors are parameterized as a function of p_{T} and η. Detector simulations are used to correct for the change in the isolation transfer factor between track selections with at least 8 SCT hits to those passing the disappearing track condition.

Since the electron and hadronic scattering backgrounds have similar pixel tracklet p_{T} shapes, the electron transfer factors are used to obtain templates for the hadronic scattering backgrounds. A single inner detector track control region is used in Equation 1 instead of $N^{\mathrm{CR}}_{e,\mathrm{signal}}$. Similar to the electron $\mathrm{TF}^{e}_{\mathrm{calo-veto}}$, detector simulations are used to correct for the length of the track. Corrections are derived using simulated single pion events for the hadronic scattering backgrounds.

Similar to the electron measurement, the muon transfer factors are factorized into two components: pixel tracklet and no MS track association, and multiplied by the number of events in the single muon control region to estimate the number of muon scattering backgrounds,

$$f^{\mu}_{SR}(p_{\mathrm{T}},\eta,\phi) = N^{\mathrm{CR}}_{\mu,\mathrm{signal}}(p_{\mathrm{T}},\eta,\phi) \times \mathrm{TF}^{\mu}_{\mathrm{pixel-only}}(p_{\mathrm{T}},\eta) \times \mathrm{TF}^{\mu}_{\mathrm{noMStrack}}(\eta,\phi),$$

where $N^{\mathrm{CR}}_{\mu,\mathrm{signal}}$ is the number of events in the single-muon CR, $\mathrm{TF}^{\mu}_{\mathrm{pixel-only}}$ is the transfer factor representing the probability for muons to be mis-identified as a pixel tracklet, and $\mathrm{TF}^{\mu}_{\mathrm{noMStrack}}$ is the transfer factor accounting for the probability that a muon with a good inner detector track does not have an associated MS track.

In the muon pixel tracklet measurement, the probe lepton is a muon track reconstructed only in the MS detector. The transfer factor $\mathrm{TF}^{\mu}_{\mathrm{pixel-only}}$ is calculated in the same way as the electron pixel transfer factor, but the denominator is the number of events where the probe is matched to a muon. The no MS track transfer factor $\mathrm{TF}^{\mu}_{\mathrm{noMStrack}}$ uses a high quality inner detector track as the probe. It assesses the probability for an MS track to not be geometrically matched to an inner detector track. In order to account for the detector geometry, the transfer factor is measured as a function of η and ϕ. No significant p_{T} dependence is observed.

6.3 Smearing functions

The transverse momentum resolution of a track scales as $\Delta p_{\mathrm{T}}/p_{\mathrm{T}} \propto 1/L^{2}_{\mathrm{T}}$, where L_{T} is the transverse length of the track's trajectory. Since pixel tracklets only have pixel hits, they will be significantly shorter than tracks with a full set of pixel, SCT and TRT hits, and thus the transverse momentum resolution of the pixel tracklets will be significantly worse than full length tracks. Therefore, the templates constructed from tracks in the control regions need to be smeared to match the pixel tracklet momentum resolution. Additionally, the tracklet q/p_{T} resolution, where q is the electric charge of the track or pixel tracklet, measured using observed data samples is worse than that predicted by simulation, and measurements in data are used to correct simulated predictions.

The q/p_{T} resolution strongly depends on the momentum of the track: at low momentum, multiple scattering effects are dominant, while at higher momentum the alignment of the detector can affect the resolution. Since a fit is performed to the shape of the pixel tracklet p_{T} spectrum, it is important to have a good description of the different components of the spectrum. The measured tracklet resolution in data is used to correct the shapes of the track p_{T} templates in the control regions, and additionally correct the expected q/p_{T} resolution of the simulated signal predictions to match the data.

Smearing functions are derived using $Z \to \mu\mu$ and $Z \to ee$ events. Events are selected from a filtered data stream designed to select $Z \to \ell\ell$ events. They are required to satisfy the data quality criteria described in Section 3, and contain two same-flavour leptons with an invariant mass between 81 GeV and 101 GeV. Driven by the threshold applied to the filter, the transverse momenta of the leading and sub-leading leptons are required to be greater 25 GeV. A specialised track reconstruction configuration is then used to re-track the leptons using pixel hits only, and the re-tracked leptons are used to derive a q/p_T smearing function with respect to the lepton four-momentum.

The $\Delta(q/p_T)$ distribution is fitted using an approximate double-sided crystal-ball function [49, 50]:

$$f(z) = \begin{cases} \exp(\alpha(z+\alpha/2)) & (z < -\alpha) \\ \exp(-z^2/2) & (-\alpha < z < \alpha), \\ \exp(-\alpha(z-\alpha/2)) & (z > \alpha) \end{cases}$$
$$z = \frac{\Delta(q/p_T) - \beta}{\sigma},$$

where α, β, and σ are parameters controlling the slope of the tail part, and the mean and resolution of the core part of the distribution respectively. The parameter σ has a significant p_{T} dependence, and parameters are measured in data for $p_{\mathrm{T}} > 25$ GeV. Smearing functions estimated using the detector simulation are used for tracks with transverse momentum down to $p_{\mathrm{T}} > 10$ GeV. The predictions of the smearing parameters above 25 GeV are used to correct the overall scale difference between data and simulation, and to correct the parametrisation obtained with the simulation below 25 GeV. The p_{T} dependent smearing function parameters derived for electrons and muons are shown in Table 4.

Table 4: The p_{T} dependent σ and α smearing parameters for muons and electrons. The mean β parameter is fixed to zero.

	Muon		Electron	
Transverse momentum	σ [TeV^{-1}]	α	σ [TeV^{-1}]	α
$10 < p_{\mathrm{T}} < 15$	16.96	1.72	20.94	1.86
$15 < p_{\mathrm{T}} < 20$	15.54	1.72	19.54	1.86
$15 < p_{\mathrm{T}} < 25$	14.91	1.72	18.33	1.86
$25 < p_{\mathrm{T}} < 35$	14.84	1.72	17.01	1.86
$35 < p_{\mathrm{T}} < 45$	14.21	1.66	15.42	1.82
$45 < p_{\mathrm{T}} < 60$	13.64	1.62	14.49	1.66
$60 < p_{\mathrm{T}} < 100$	13.44	1.68	13.90	1.54
$100 < p_{\mathrm{T}}$	13.21	1.64	14.03	1.64

6.4 Combinatorial fake backgrounds

Fake tracks are reconstructed from an unassociated combination of hits. These tracks can have high transverse momentum and can mimic the signal. Since their d_0 is broadly distributed, whereas the high-p_{T}

chargino tracks have good pointing resolution and originate from the primary interaction region, the high d_0 sidebands can be used as a control region pure in fake tracks. A control sample of pure fake tracks is obtained by applying the same kinematic selection requirements as in the signal region, but without the offline $E_{\mathrm{T}}^{\mathrm{miss}}$ selection to increase statistics, and with an inverted cut on the transverse impact parameter of $|d_0/\sigma_{d_0}| > 10$.

The p_{T} spectrum of mis-measured pixel tracklet in the fake control region is modelled with the following functional form:

$$f\left(p_{\mathrm{T}}\right) = \exp\left(-p_0 \cdot \log(p_{\mathrm{T}}) - p_1 \cdot (\log(p_{\mathrm{T}}))^2\right),$$

where p_0 and p_1 satisfy the following empirical relation: $p_1 = 0.18 - 0.11 \cdot p_0$. In order to break any correlations between p_0 and p_1 in the fit described in Section 6.5, the parameters are rotated by an angle θ and redefined as $p_0 = p_0' \cos\theta - p_1' \sin\theta$ and $p_1 = p_0' \sin\theta + p_1' \cos\theta$. The θ value is chosen such that the two parameters are uncorrelated, and found to be $\theta = -0.0973$. The p_0 and p_1 parameters are determined in the combined fit described in Section 6.5. The parameter p_1 is found to be $p_1 = 0.171 \pm 0.002$ in both signal region channels, and $p_0 = 1.172 \pm 0.113$ (0.996 ± 0.110) in the electroweak (strong) channels. The data and fitted fake background are shown in Figure 4 for the electroweak and strong production fake control regions, showing a good agreement between the fit and the data.

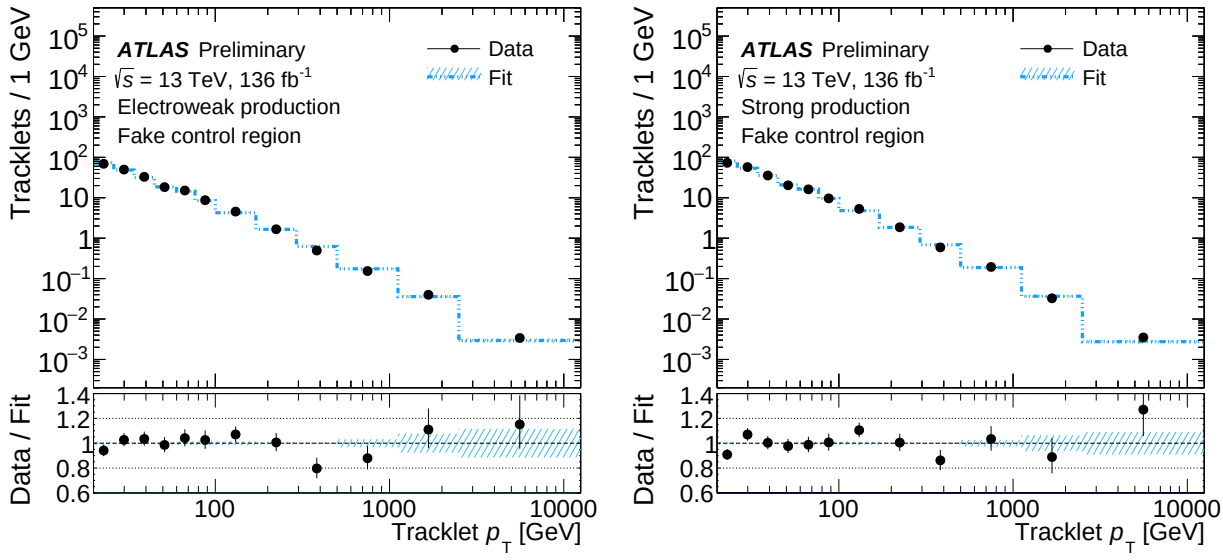

(a) (b)

Figure 4: Fit in the fake-tracklet control sample for (a) the electroweak production channel and (b) the strong production channel. The black markers show data. The blue line and the hashed band show the fit function and its uncertainty. The bottom insert shows the ratio of the data to the fitted prediction.

6.5 Fitting procedure

The background estimation is performed by fitting the high-$E_{\mathrm{T}}^{\mathrm{miss}}$ signal region or the middle-$E_{\mathrm{T}}^{\mathrm{miss}}$ validation region, simultaneously with the low-$E_{\mathrm{T}}^{\mathrm{miss}}$ and fake-tracklet control regions described in Section 6.1. The fit is performed using the likelihood function described in the following.

The likelihood function for the tracklet p_{T} ($\mathcal{L}$) in a sample of observed events (N_{obs}) is defined as $\mathcal{L} = \mathcal{L}_{\mathrm{shape}} \times \mathcal{L}_{\mathrm{shape}}^{\mathrm{Fake\,CR}} \times \mathcal{L}_{\mathrm{syst}}$. The shape terms represents the probability to observe N_{obs} events in the low-$E_{\mathrm{T}}^{\mathrm{miss}}$ and high-$E_{\mathrm{T}}^{\mathrm{miss}}$ region. The $\mathcal{L}_{\mathrm{shape}}$ term is defined in Equation 2 as:

$$\mathcal{L}_{\mathrm{shape}} = \prod_{R}^{\text{low-/high-}E_{\mathrm{T}}^{\mathrm{miss}}} \mathcal{L}_{\mathrm{shape}}^{R}\,, \tag{2}$$

with

$$\mathcal{L}_{\mathrm{shape}}^{R} = \frac{\exp\left(-\sum_{i}^{s,e,\mu,h,c} n_i^R\right)}{N_{\mathrm{obs}}^R\,!} \times \prod_{N_{\mathrm{obs}}^R} \left(\sum_{i'}^{s,e,\mu,h} \left(n_{i'}^R \cdot f_{i'}^R(p_{\mathrm{T}}; \sigma_{i'}, \alpha_{i'}) \right) + n_c^R \cdot f_c(p_{\mathrm{T}}; p_0, p_1) \right), \tag{3}$$

and the $\mathcal{L}_{\mathrm{shape}}^{\mathrm{Fake\,CR}}$ term is defined in Equation 4 as:

$$\mathcal{L}_{\mathrm{shape}}^{\mathrm{Fake\,CR}} = \frac{\exp\left(-n_c^{\mathrm{Fake\,CR}}\right)}{N_{\mathrm{obs}}^{\mathrm{Fake\,CR}}\,!} \times \prod_{N_{\mathrm{obs}}^{\mathrm{Fake\,CR}}} \left(n_c^{\mathrm{Fake\,CR}} \cdot f_c(p_{\mathrm{T}}; p_0, p_1) \right), \tag{4}$$

where s, e, μ, h and c are subscripts of the signal process, the electron, the muon, the hadron and the combinatorial fake-tracklet backgrounds respectively; N_{obs}^R is the number of observed events in each of the fitted regions, R = high-$E_{\mathrm{T}}^{\mathrm{miss}}$ or low-$E_{\mathrm{T}}^{\mathrm{miss}}$ region; n_i^R is the number of estimated events of process i in region R, $\sigma_{i'}$ and $\alpha_{i'}$ are the smearing parameters of process i'; p_0 and p_1 are the parameters for the combinatorial fake-tracklet background fit described in the Section 6.4; f_i is the charged particle scattering background shape template for process i described in Sections 6.2 and 6.3; n_c^R are estimated number of events in region R and $n_c^{\text{low-}E_{\mathrm{T}}^{\mathrm{miss}}}$ is a free parameter in the likelihood fit, $n_c^{\text{high-}E_{\mathrm{T}}^{\mathrm{miss}}}$ is defined by in Equation 5 as:

$$n_c^{\text{high-}E_{\mathrm{T}}^{\mathrm{miss}}} = r_{\mathrm{CD}} \cdot \exp(r_{\mathrm{ABCD}}) \cdot n_c^{\text{low-}E_{\mathrm{T}}^{\mathrm{miss}}}, \tag{5}$$

with r_{CD} defined in Equation 6 as:

$$r_{\mathrm{CD}} = \frac{n_c^{\text{high-}E_{\mathrm{T}}^{\mathrm{miss}}\ \mathrm{Fake\,CR}}}{n_c^{\text{low-}E_{\mathrm{T}}^{\mathrm{miss}}\ \mathrm{Fake\,CR}}}, \tag{6}$$

and r_{ABCD} defined in Equation 7 as:

$$r_{\mathrm{ABCD}} = \ln \frac{n_c^{\text{high-}E_{\mathrm{T}}^{\mathrm{miss}}} / n_c^{\text{high-}E_{\mathrm{T}}^{\mathrm{miss}}\ \text{Fake CR}}}{n_c^{\text{low-}E_{\mathrm{T}}^{\mathrm{miss}}} / n_c^{\text{low-}E_{\mathrm{T}}^{\mathrm{miss}}\ \text{Fake CR}}}, \tag{7}$$

where r_{CD} and r_{ABCD} are terms to constrain the combinatorial fake-tracklet background between the low-$E_{\mathrm{T}}^{\mathrm{miss}}$ CR and the high-$E_{\mathrm{T}}^{\mathrm{miss}}$ SR, and $n_c^{\mathrm{Fake\,CR}}$ is an estimated number of events in the fake control region described in the Table 3, which is a free parameter.

$\mathcal{L}_{\mathrm{syst}}$ consists of a product of terms related to the systematic uncertainties in each background process and the signal process, $\mathcal{L}_{\mathrm{syst}} = \mathcal{L}^s_{\mathrm{syst}} \times \mathcal{L}^e_{\mathrm{syst}} \times \mathcal{L}^\mu_{\mathrm{syst}} \times \mathcal{L}^h_{\mathrm{syst}} \times \mathcal{L}^c_{\mathrm{syst}}$. Each likelihood components is defined as below,

$$\begin{aligned}
\mathcal{L}^s_{\mathrm{syst}} &= \mathrm{Gaus}\left(\sigma_s; \overline{\sigma_s}, \Delta\sigma_s\right) \times \mathrm{Gaus}\left(\alpha_s; \overline{\alpha_s}, \Delta\alpha_s\right) \times \prod_R \mathrm{Gaus}\left(n_s^R; \overline{n_s^R}, \Delta n_s^R\right), \\
\mathcal{L}^\mu_{\mathrm{syst}} &= \mathrm{Gaus}\left(\sigma_\mu; \overline{\sigma_\mu}, \Delta\sigma_\mu\right) \times \mathrm{Gaus}\left(\alpha_\mu; \overline{\alpha_\mu}, \Delta\alpha_\mu\right) \times \prod_R \mathrm{Gaus}\left(n_\mu^R; \overline{n_\mu^R}, \Delta n_\mu^R\right), \\
\mathcal{L}^e_{\mathrm{syst}} &= \mathrm{Gaus}\left(\sigma_e; \overline{\sigma_e}, \Delta\sigma_e\right) \times \mathrm{Gaus}\left(\alpha_e; \overline{\alpha_e}, \Delta\alpha_e\right) \times \prod_R \mathrm{Gaus}\left(n_e^R; \overline{n_e^R}, \Delta n_e^R\right), \\
\mathcal{L}^h_{\mathrm{syst}} &= \mathrm{Gaus}\left(\sigma_h; \overline{\sigma_h}, \Delta\sigma_h\right) \times \mathrm{Gaus}\left(\alpha_h; \overline{\alpha_h}, \Delta\alpha_h\right), \\
\mathcal{L}^c_{\mathrm{syst}} &= \mathrm{Gaus}\left(r_{\mathrm{ABCD}}; 1, \Delta r_{\mathrm{ABCD}}\right),
\end{aligned}$$

where $\mathrm{Gaus}(a; b, c)$ represents a unit Gaussian function of a with a mean of b and a standard deviation c. The expected value and the uncertainty of a variable x is represented by $\overline{x}$ and Δx respectively.

The likelihood is maximised by minimising the negative log likelihood function with the MINUIT [51] package and the RooFit framework [52]. The fit parameters are the normalisations of the hadron and the combinatorial fake-tracklet backgrounds(n_h^R and n_c^R), p_0 and p_1 which are parameters of the fit to the fake-tracklet transverse momentum distribution described in Section 6.4, and nuisance parameters. The nuisance parameters are allowed to float in the fit with a Gaussian constraint to include sources of systematics uncertainties. The statistical uncertainty in the transfer factors for electrons and muons is propagated into the final template.

7 Systematic Uncertainties

Several sources of uncertainties are considered for this search, and can be divided into uncertainties affecting the parameters in the background and signal fit model, and those affecting the expected signal yields.

7.1 Fit Model Uncertainties

Uncertainties in the normalization of the electron and muon backgrounds are dominated by the uncertainties of the transfer factors. The shape uncertainty in the hadron and charged-lepton backgrounds is dominated by uncertainties in the smearing functions. The pile-up condition is the largest source of the uncertainty of the smearing function especially for lower p_{T} tracklets. The pile-up uncertainty is evaluated by taking the difference between the nominal value of the smearing parameters and the values obtained from events with different pile-up conditions. The dataset is split into low ($\mu < 40$) and high ($\mu > 40$) pile-up conditions, and the full difference between the low and high datasets are assigned as a systematic uncertainty on the p_{T} dependent smearing parameters.

The uncertainties in r_{CD} and r_{ABCD} are obtained from statistical uncertainties in the control regions used to calculate these parameters. An additional uncertainty on the extrapolation of r_{ABCD} over $d_0/\sigma(d_0)$ is obtained by evaluating r_{ABCD} using pixel tracklets with $3 < d_0/\sigma(d_0) < 10$ for $n_c^{\text{high-}\mathrm{E_T^{miss}}}$ and $n_c^{\text{low-}\mathrm{E_T^{miss}}}$ in Equation 7. Since fake tracklets are the dominant backgrounds in the signal regions, variations of these parameters are the leading source of uncertainty in both the electroweak and strong production signal regions. Similarly, the p_0 and p_1 parameters are varied up and down by their statistical uncertainties obtained from the fit.

Table 5 summarises the effect of various sources of systematic uncertainties on the signal exclusion significance.

	Electroweak channel [%]	Strong channel [%]
r_{ABCD}	5.2	0.9
r_{CD}	3.2	0.6
σ in signal p_{T} smearing function	2.9	0.1
α in signal p_{T} smearing function	1.7	0.2
p_0 parameter in the fake background p_{T} function	0.3	<0.1
p_1 parameter in the fake background p_{T} function	0.3	0.2
Normalization of muon background	0.6	<0.1
Normalization of electron background	<0.1	<0.1
α in muon p_{T} smearing function	<0.1	<0.1
σ in muon p_{T} smearing function	<0.1	<0.1
α in electron p_{T} smearing function	<0.1	<0.1
σ in electron p_{T} smearing function	<0.1	<0.1
α in hadron p_{T} smearing function	0.5	0.2
σ in hadron p_{T} smearing function	0.6	0.2

Table 5: Effects of systematic uncertainties on the signal exclusion significance for a representative signal point with $m_{\tilde{\chi}_1^\pm} = 600$ GeV for the electroweak channel and $m_{\tilde{g}} = 1400$ GeV and $m_{\tilde{\chi}_1^\pm} = 1100$ GeV for the strong channel.

7.2 Signal Uncertainties

A breakdown of the systematic uncertainties for the expected number of signal events in the signal regions is shown in Table 6.

Theoretical uncertainties in the signal cross-section are estimated in a way similar to the previous result [14]. This is done by computing the changes in the cross-section when the renormalisation and factorisation scales, the choice of PDFs and the strong coupling constant, α_S, are varied independently. Renormalisation

and factorisation scales are varied by factors of 0.5 and 2 from their nominal value. The PDF uncertainty is estimated as the maximum of the uncertainty from the CTEQ6.6 [53] uncertainty band at 68% confidence level and the difference between CTEQ6.6 and MSTW2008 NLO PDF [54] sets. Each uncertainty is varied independently and their effects are added in quadrature. Uncertainties in the modelling of ISR and final state radiation (FSR) are estimated by varying the renormalisation, factorisation and merging scales from 0.5 to 2 times their nominal values, and by comparing samples with additional partons in the matrix element with MG5_aMC@NLO+Pythia8. Jet modelling uncertainties related to energy scale and resolution, and jet vertex tagging are estimated by comparing simulated events and data as described in Ref. [43]. The pile-up modelling uncertainty is estimated by varying the number of collisions per bunch crossing in simulation by its uncertainty of 10% of the nominal value. The uncertainty in the $E_{\mathrm{T}}^{\mathrm{miss}}$ soft term modelling is considered by comparing data and simulated samples using $Z \rightarrow \mu\mu$ + jets events as described in Ref. [45]. The uncertainty in the trigger efficiency modelling is small because it is measured from data as described in Section 5. Only the statistical uncertainty in the efficiency measurement is taken into account as the signal trigger efficiency uncertainty.

The uncertainty in the tracklet reconstruction efficiency is split into two components. First, the uncertainty in the probability for a tracklet to produce a set of pixel-detector hits which can satisfy the tracklet quality selection. Second, the uncertainty in the efficiency to reconstruct a tracklet when it contains set of good hits that satisfy the remaining tracklet quality selection. These uncertainties are derived using the re-tracked lepton data sample described in Section 6.3.

	Electroweak channel [%] $m_{\tilde{\chi}_1^\pm}$ = 600 GeV	Strong channel [%] $m_{\tilde{g}}$ = 1400 GeV $m_{\tilde{\chi}_1^\pm}$ = 1100 GeV
Cross-section	7.6	14
Initial/final state radiation	8.4	5.1
Jet energy scale	2.3	1.5
Jet energy resolution	0.6	0.3
Jet vertex tagging efficiency	<0.1	<0.1
Pile-up modelling	0.7	<0.1
$E_{\mathrm{T}}^{\mathrm{miss}}$ soft term	0.4	<0.1
Trigger efficiency	0.3	0.4
Tracklet reconstruction efficiency	5.9	
Luminosity	1.7	
Total	11	8.1

Table 6: Effects of systematic uncertainties in the signal yields for representative signal points with $\tau_{\tilde{\chi}_1^\pm}$ = 0.2 ns. All values are symmetrised using the largest variation of one standard deviation with respect to the expected signal yields. The uncertainty on the pixel tracklet efficiency and the luminosity are common across the two signal regions.

8 Results and interpretation

The transverse momentum spectra of the fitted pixel tracklets in the low-$E_{\mathrm{T}}^{\mathrm{miss}}$, the calorimeter sideband CR and middle-$E_{\mathrm{T}}^{\mathrm{miss}}$ and high-$E_{\mathrm{T}}^{\mathrm{miss}}$ regions for the electroweak and strong production channels are shown in Figures 5 and 6, respectively. Examples of the expected signal prediction with $m_{\tilde{\chi}_1^\pm}$ = 600 GeV and $\tau_{\tilde{\chi}_1^\pm}$ = 0.2 ns for the electroweak production, and $m_{\tilde{g}}$ = 1400 GeV, $m_{\tilde{\chi}_1^\pm}$ = 1100 GeV for the strong production channel are overlaid in red.

The number of events in the validation regions is shown in Table 7. Good agreement is observed between data and background predictions in all validation regions. No significant excess above the background predictions is observed in the high-$E_{\mathrm{T}}^{\mathrm{miss}}$ signal regions as shown in Table 8. The probability of a background-only experiment being more signal-like than observed (p_0), its equivalent formulation in terms of the number of standard deviations (Z), and the upper limit on the model-independent visible cross-section at 95% CL using the CLs technique [55] are also shown in Table 8.

	Electroweak channel		Strong channel	
	Middle-$E_{\mathrm{T}}^{\mathrm{miss}}$ VR			
	Calo side-band $p_{\mathrm{T}} > 60$ GeV	Low p_{T} $p_{\mathrm{T}} < 60$ GeV	Calo side-band $p_{\mathrm{T}} > 60$ GeV	Low p_{T} $p_{\mathrm{T}} < 60$ GeV
Fake	4.3 ± 2.2	5.5 ± 1.5	3.2 ± 1.5	3.5 ± 1.0
Hadron	1.0 ± 0.8	23 ± 6	0.36 ± 0.23	13 ± 4
Electron	0.8 ± 0.5	1.2 ± 1.3	0.29 ± 0.20	0.5 ± 0.5
Muon	0.023 ± 0.007	0.25 ± 0.06	0.012 ± 0.004	0.129 ± 0.032
Total Expected	6.1 ± 1.9	29 ± 5	3.8 ± 1.5	17 ± 4
Observed	5	30	3	18

Table 7: Expected and observed number of events and corresponding background predictions in the validation regions. The uncertainty on the total background prediction is different than the quadratic sum of the individual components due to anti-correlation of fit parameters between the backgrounds.

	Electroweak channel	Strong channel
	High-$E_{\mathrm{T}}^{\mathrm{miss}}$ SR	
Fake	2.6 ± 0.8	0.77 ± 0.33
Hadron	0.26 ± 0.13	0.024 ± 0.031
Electron	0.021 ± 0.023	0.004 ± 0.004
Muon	0.17 ± 0.06	0.049 ± 0.018
Total Expected	3.0 ± 0.7	0.84 ± 0.33
Observed	3	1
p_0 (Z)	0.5 (0)	0.38 (0.30)
Observed $\sigma_{\mathrm{vis}}^{95\%}$ [fb]	0.037	0.028
Expected $\sigma_{\mathrm{vis}}^{95\%}$ [fb]	$0.038\ ^{+0.014}_{-0.009}$	$0.024\ ^{+0.009}_{-0.003}$

Table 8: Expected and observed number of events and corresponding background predictions in the signal regions with transverse momenta above 60 GeV. The uncertainty on the total background prediction is different than the quadratic sum of the individual components due to anti-correlation of fit parameters between the backgrounds.

Model-dependent exclusion limits at 95% confidence level (CL) are placed on the various signal models. The likelihood function is expanded to contain both signal and background components. The signal normalization is the parameter of interest and is unconstrained in the fit. For the electroweak production of pure winos or pure higgsinos, the exclusion limits are shown as a function of the chargino lifetime and mass. In the case of pure winos, chargino masses are excluded up to 660 GeV as shown in Figure 7, in

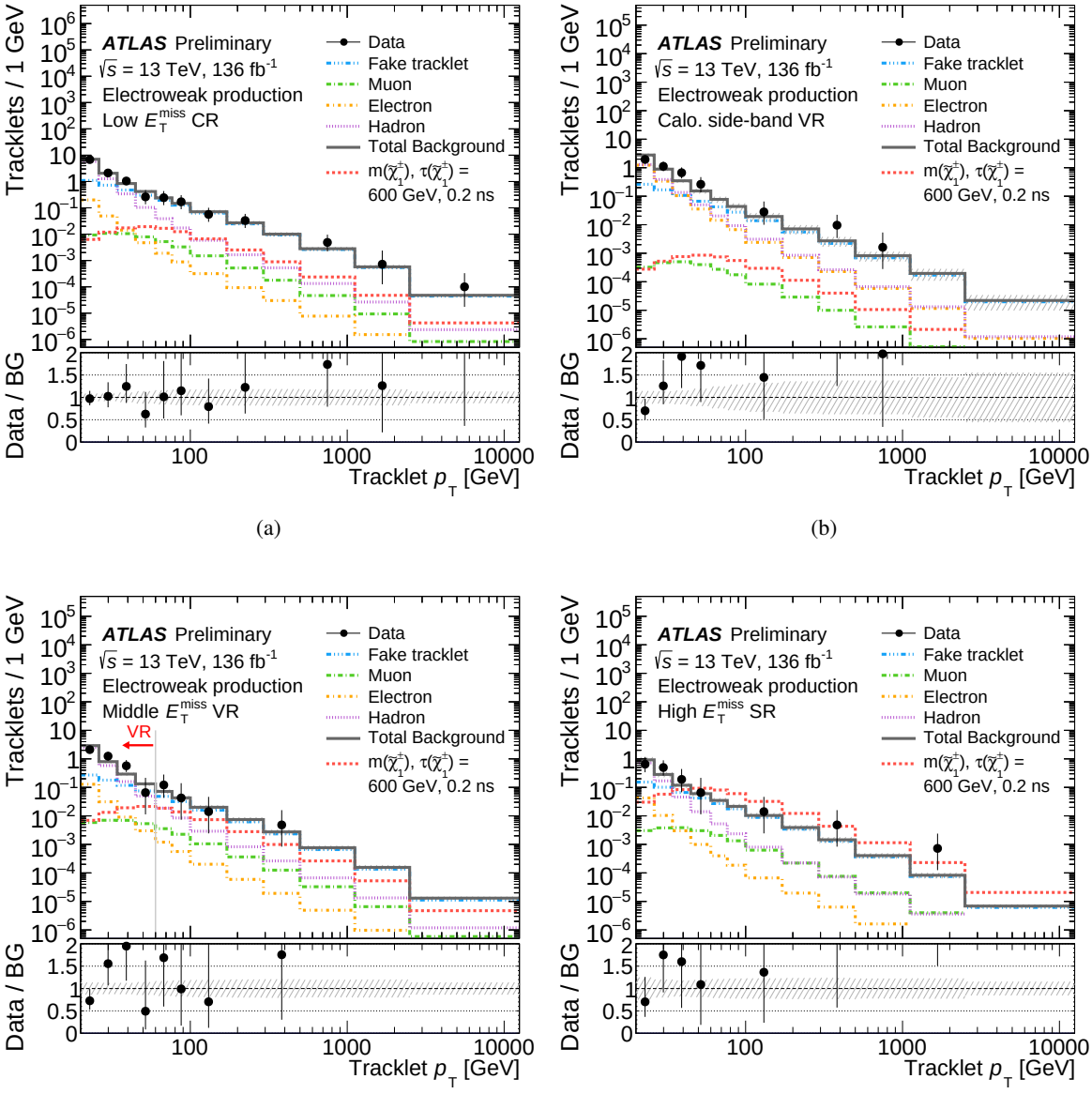

Figure 5: Pixel tracklet p_{T} spectrum fit results in the low-, middle- and high-$E_{\mathrm{T}}^{\mathrm{miss}}$ regions for electroweak production channel. Backgrounds shown by the various lines are fit to observed data events in a background-only fit. An example of the expected signal prediction with $m_{\tilde{\chi}_1^\pm} = 600$ GeV and $\tau_{\tilde{\chi}_1^\pm} = 0.2$ ns in overlaid in red. The last bin includes overflow entries. The bottom panel shows the ratio of data to the background-only prediction.

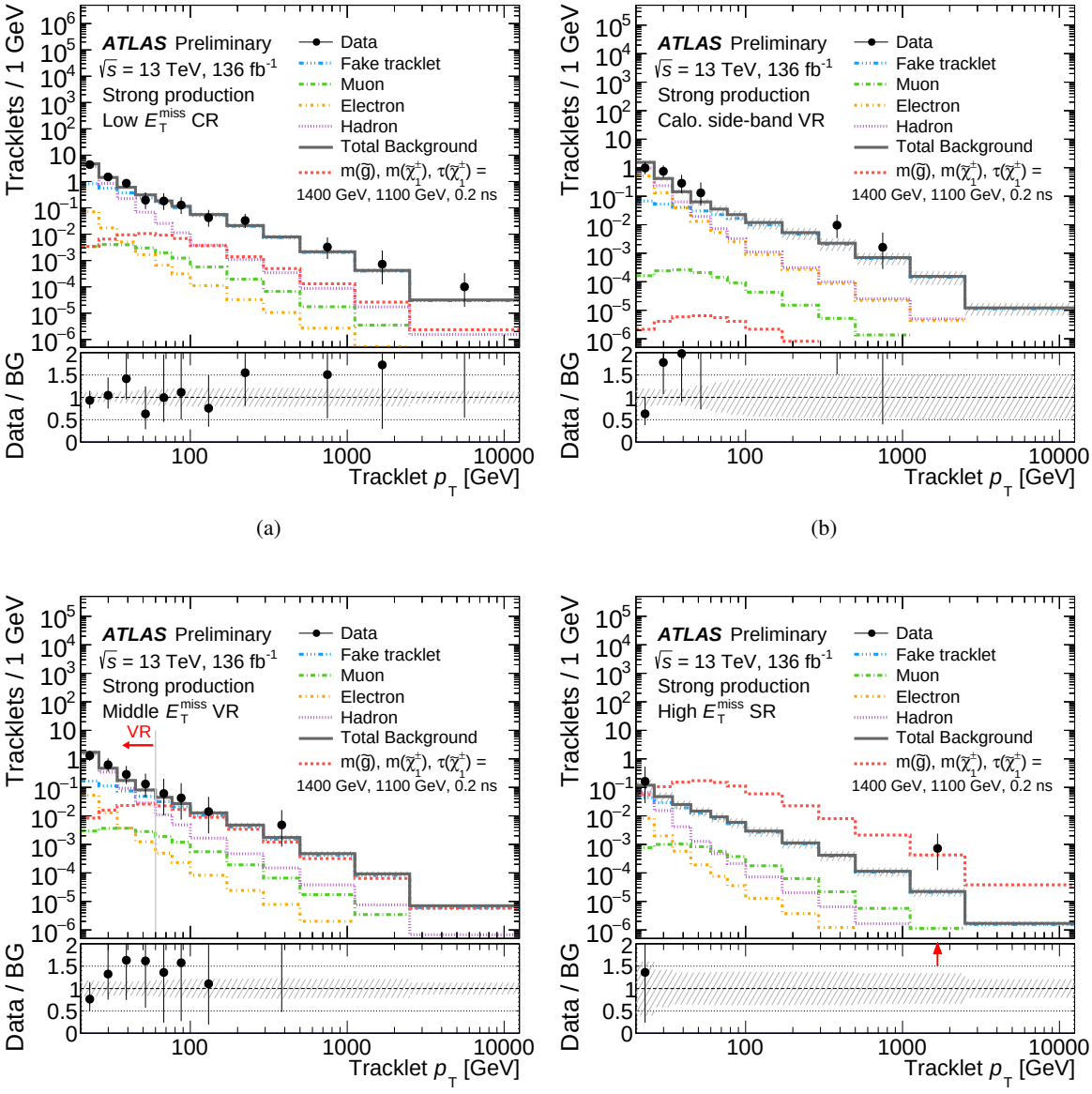

Figure 6: Pixel tracklet p_{T} spectrum fit results in the low-, middle- and high-$E_{\mathrm{T}}^{\mathrm{miss}}$ regions for the strong production channel. Backgrounds shown by the various lines are fit to observed data events in a background-only fit. An example of the expected signal prediction with $m_{\tilde{g}} = 1400$ GeV, $m_{\tilde{\chi}_1^{\pm}} = 1100$ GeV is overlaid in red. The last bin includes overflow entries. The bottom panel shows the ratio of data to the background-only prediction.

which the pure wino lifetime is shown by the grey dashed line. For pure higgsinos, chargino masses are excluded up to 210 GeV as shown in Figure 8, in which the relative sensitivity difference between the higgsinos and winos is explained by two factors: the smaller production cross-section of higgsinos relative to the wino case, and the extremely short lifetime of the higgsinos. For the strong production channels, the exclusion limits are set as a function of the lightest chargino mass and the gluino mass. The exclusion limits for charginos with lifetimes fixed to 0.2 ns and 1.0 ns are shown in Figure 9. Gluino masses are excluded beyond 2 TeV for chargino masses up to 600 GeV. Chargino masses below 1.4 TeV are excluded in the case of compressed spectra with a mass difference of 50 GeV between the gluino and the chargino.

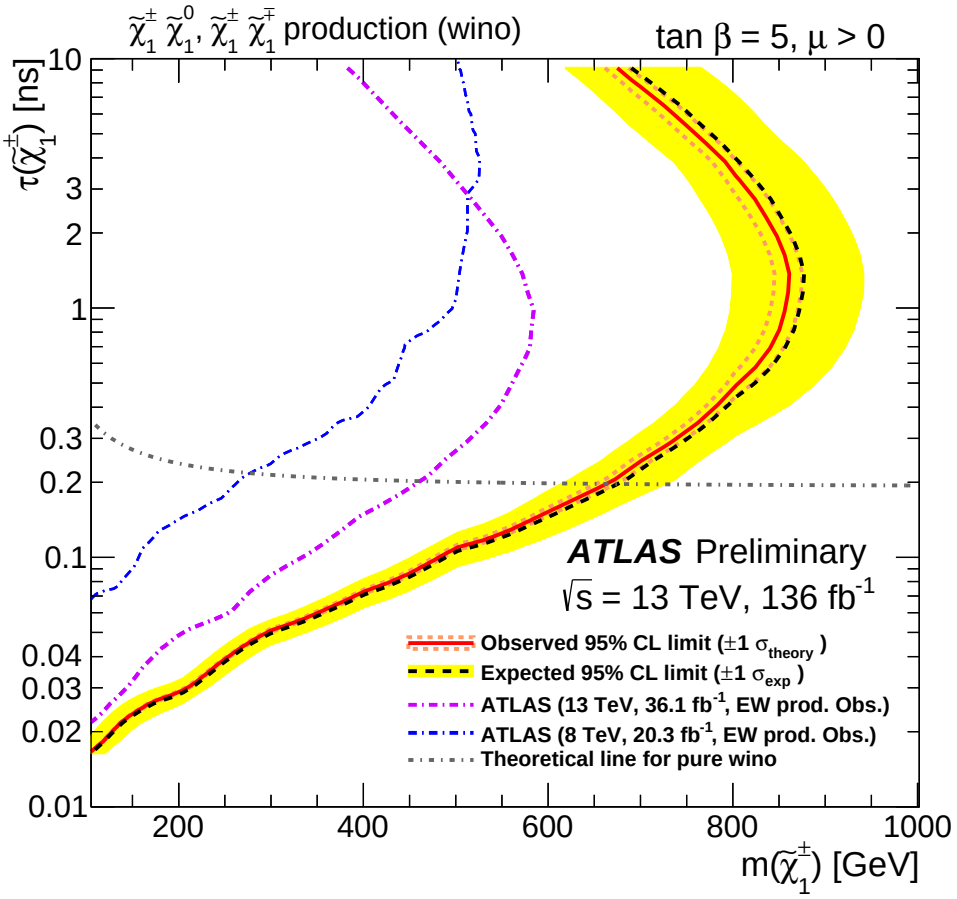

Figure 7: Exclusion limits at 95% CL obtained in the electroweak production channel with the pure wino scenario. The limits are shown as a function of the chargino lifetime and mass. The black dashed line shows the median value, and the yellow band shows the 1σ uncertainty band on the expected limits. The red line shows the observed limits and the red dotted lines, the corresponding 1σ uncertainty on the signal cross-section. The blue and violet broken lines show the observed limits from the ATLAS results [14] and [16] respectively.

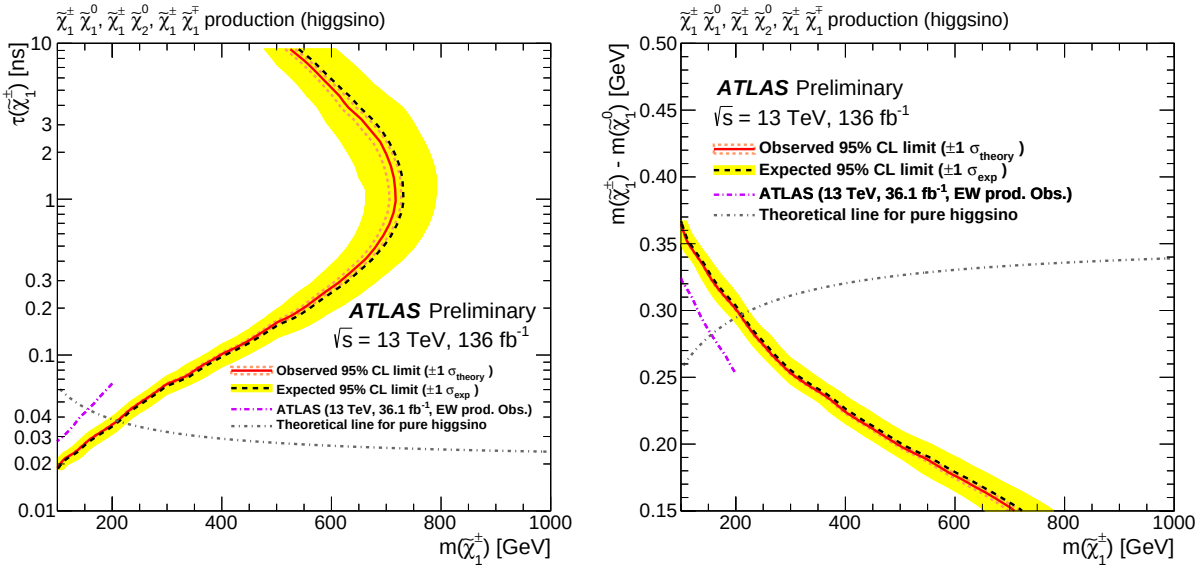

(a) (b)

Figure 8: Exclusion limits at 95% CL obtained in the electroweak production channel with the pure higgsino scenario. The limits are shown separately for the higgsino lifetime or mass splitting as a function of the chargino mass. The black dashed line shows the median value, and the yellow band shows the 1σ uncertainty band on the expected limits. The red line shows the observed limits and the red dotted lines, the corresponding 1σ uncertainty on the signal cross-section. The violet broken line shows the observed limits from the ATLAS result [15].

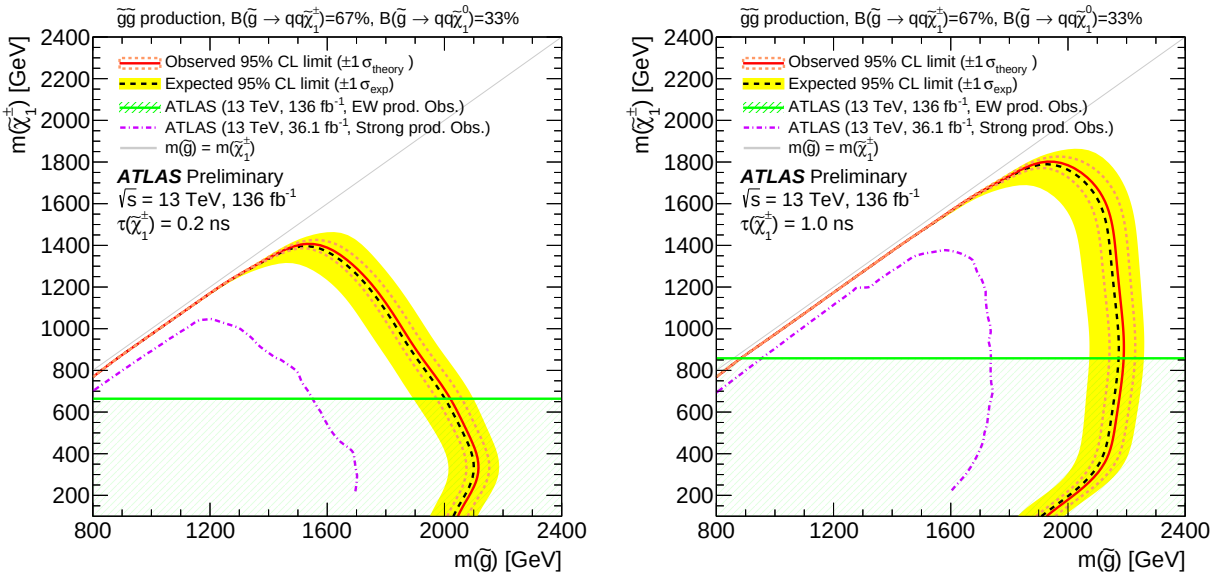

(a) (b)

Figure 9: Exclusion limits at 95% CL obtained in the strong production channel. The limits are shown as function of the lightest chargino mass vs the gluino mass, for chargino lifetimes of 0.2 ns (a) and 1.0 ns (b). The black dashed line shows the median value, and the yellow band shows the 1σ uncertainty band on the expected limits. The red line shows the observed limits and the red dotted lines, the corresponding 1σ uncertainty on the signal cross-section. The observed exclusion limit from this search in direct electroweak wino production channel with $\tau_{\tilde{\chi}_1^{\pm}}$ = 0.2 ns (a) and 1.0 ns (b) is overlaid in green.

9 Conclusion

A search for long-lived charginos with a disappearing track signature was performed using $\sqrt{s} = 13$ TeV pp collision data collected by the ATLAS experiment, corresponding to an integrated luminosity of 136 fb^{-1}. Pixel tracklets with at least four hits in the pixel detector are used to improve the sensitivity for short chargino lifetimes. A strong disappearing track condition, enforced by a veto on SCT hits and no significant calorimeter energy in the tracklets trajectory, has been developed specifically for this search and is used to significantly reduce background processes. The improved background rejection that this disappearing track condition offers, together with over a factor of three increase in integrated luminosity, has allowed the ATLAS Collaboration to significantly improve sensitivity to long-lived charginos. A lower limit on chargino masses for electroweak production of long-lived charginos in pure wino (higgsino) models is set at 660 (210) GeV at 95% CL. If charginos with a proper lifetime of 0.2 ns are produced in the decay cascade of pair-produced gluinos, gluino masses below 2.1 TeV are excluded for a chargino mass of 300 GeV. Chargino masses below 1.4 TeV are excluded in the case of compressed spectra with a mass difference of 50 GeV between the gluino and the chargino.

Appendix

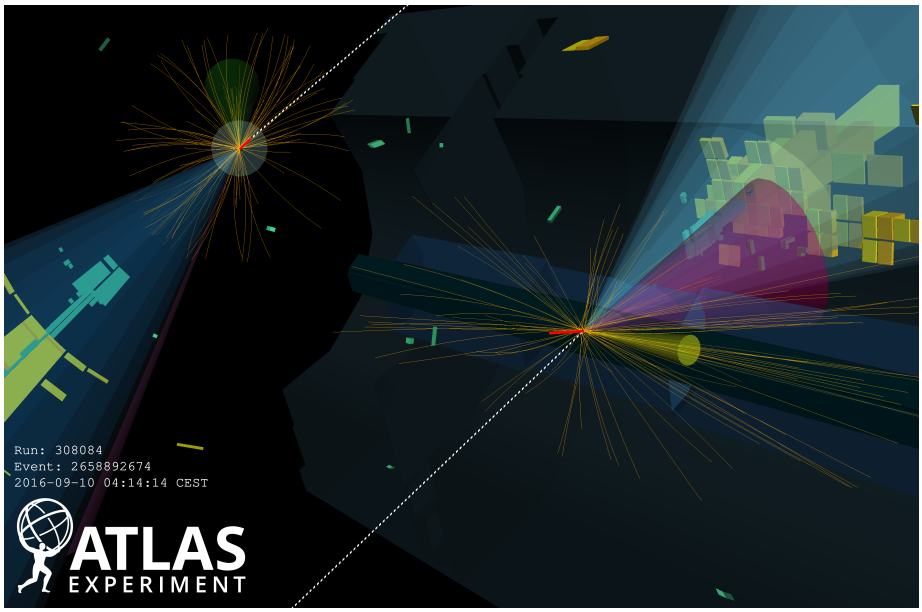

(a)

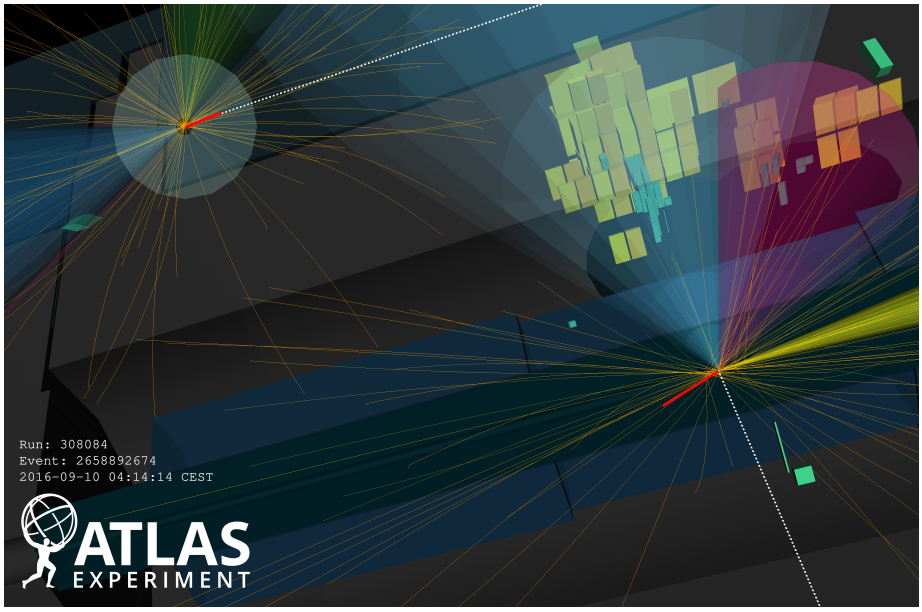

(b)

Figure 10: Event display in the signal region from data taken in 2018. The pixel tracklet candidate with $p_{\mathrm{T}} = 1.2$ TeV is shown by the red solid line and other inner detector tracks by the thin orange lines. Jets are shown by the transparent yellow, blue, and red cones. The missing transverse momentum is shown by the white dotted line. The green and yellow bars indicate energy deposits in the Liquid Argon and Scintillating Tile calorimeters respectively. The event is common to both the electroweak and strong production signal regions. Event and run numbers are shown in the bottom left corner.

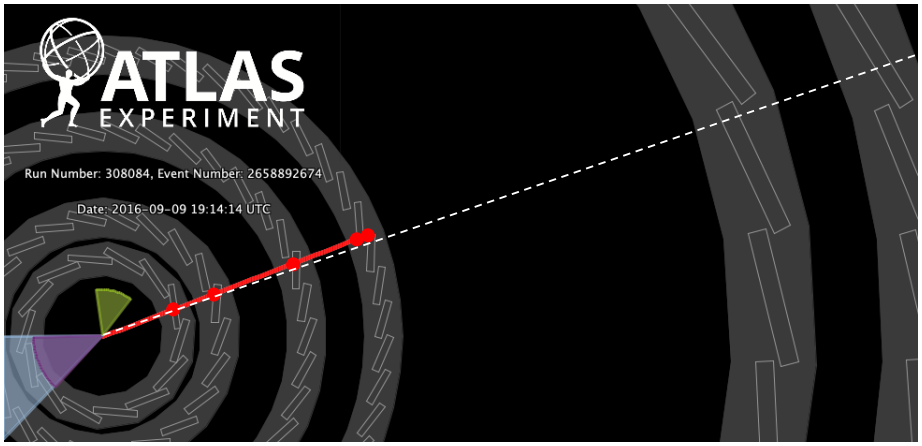

Figure 11: Event display in the signal region from data taken in 2018. The pixel tracklet candidate with $p_{\mathrm{T}} = 1.2$ TeV is shown by the red solid line. Jets are shown by the transparent yellow, blue, and red cones. The missing transverse momentum is shown by the white dotted line. Pixel modules and SCT modules are drawn in the background. The event is common to both the electroweak and strong production signal regions. Event and run numbers are shown in the top left corner.

References

[1] Y. Golfand and E. Likhtman,
Extension of the Algebra of Poincare Group Generators and Violation of P Invariance,
JETP Lett. **13** (1971) 323, [Pisma Zh. Eksp. Teor. Fiz. **13** (1971) 452] (cit. on p. 2).

[2] D. Volkov and V. Akulov, *Is the neutrino a goldstone particle?*, Physics Letters B **46** (1973) 109, ISSN: 0370-2693,
URL: http://www.sciencedirect.com/science/article/pii/0370269373904905
(cit. on p. 2).

[3] J. Wess and B. Zumino, *Supergauge transformations in four dimensions*,
Nuclear Physics B **70** (1974) 39, ISSN: 0550-3213,
URL: http://www.sciencedirect.com/science/article/pii/0550321374903551
(cit. on p. 2).

[4] J. Wess and B. Zumino, *Supergauge invariant extension of quantum electrodynamics*,
Nuclear Physics B **78** (1974) 1, ISSN: 0550-3213,
URL: http://www.sciencedirect.com/science/article/pii/0550321374901126
(cit. on p. 2).

[5] S. Ferrara and B. Zumino, *Supergauge invariant Yang-Mills theories*,
Nuclear Physics B **79** (1974) 413, ISSN: 0550-3213,
URL: http://www.sciencedirect.com/science/article/pii/0550321374905598
(cit. on p. 2).

[6] A. Salam and J. Strathdee, *Super-symmetry and non-Abelian gauges*,
Physics Letters B **51** (1974) 353, ISSN: 0370-2693,
URL: http://www.sciencedirect.com/science/article/pii/0370269374902263
(cit. on p. 2).

[7] M. Ibe, S. Matsumoto and R. Sato,
Mass Splitting between Charged and Neutral Winos at Two-Loop Level,
Phys. Lett. B **721** (2013) 252, arXiv: 1212.5989 [hep-ph] (cit. on p. 2).

[8] H. Fukuda, N. Nagata, H. Otono and S. Shirai, *Higgsino Dark Matter or Not: Role of Disappearing Track Searches at the LHC and Future Colliders*, Phys. Lett. B **781** (2018) 306,
arXiv: 1703.09675 [hep-ph] (cit. on p. 2).

[9] G. F. Giudice, M. A. Luty, H. Murayama and R. Rattazzi, *Gaugino mass without singlets*,
JHEP **12** (1998) 027, arXiv: hep-ph/9810442 (cit. on pp. 2, 5).

[10] L. Randall and R. Sundrum, *Out of this world supersymmetry breaking*,
Nucl. Phys. B **557** (1999) 79, arXiv: hep-th/9810155 (cit. on pp. 2, 5).

[11] M. Papucci, J. T. Ruderman and A. Weiler, *Natural SUSY Endures*, JHEP **09** (2012) 035,
arXiv: 1110.6926 [hep-ph] (cit. on p. 2).

[12] R. Barbieri and G. Giudice, *Upper bounds on supersymmetric particle masses*,
Nuclear Physics B **306** (1988) 63, ISSN: 0550-3213,
URL: http://www.sciencedirect.com/science/article/pii/055032138890171X
(cit. on p. 2).

[13] B. de Carlos and J. A. Casas, *One-loop analysis of the electroweak breaking in supersymmetric models and the fine tuning problem*, Phys. Lett. B **309** (1993) 320, arXiv: hep-ph/9303291
(cit. on p. 2).

[14] ATLAS Collaboration, *Search for long-lived charginos based on a disappearing-track signature in pp collisions at* $\sqrt{s} = 13$ *TeV with the ATLAS detector*, JHEP **06** (2018) 022,
arXiv: 1712.02118 [hep-ex] (cit. on pp. 3, 7, 19, 24).

[15] ATLAS Collaboration,
Search for direct pair production of higgsinos by reinterpretation of the disappearing track analysis with 36.1 fb^{-1} *of* $\sqrt{s} = 13$ *TeV data collected with the ATLAS experiment*,
ATL-PHYS-PUB-2017-019, 2017, URL: https://cds.cern.ch/record/2297480
(cit. on pp. 3, 7, 25).

[16] ATLAS Collaboration, *Search for charginos nearly mass degenerate with the lightest neutralino based on a disappearing-track signature in pp collisions at* $\sqrt{s} = 8$ *TeV with the ATLAS detector*,
Phys. Rev. D **88** (2013) 112006, arXiv: 1310.3675 [hep-ex] (cit. on pp. 3, 24).

[17] CMS Collaboration, *Search for disappearing tracks in proton–proton collisions at* $\sqrt{s} = 8$ *TeV*,
JHEP **01** (2015) 096, arXiv: 1411.6006 [hep-ex] (cit. on p. 3).

[18] ATLAS Collaboration, *The ATLAS Experiment at the CERN Large Hadron Collider*,
JINST **3** (2008) S08003 (cit. on p. 4).

[19] ATLAS Collaboration, *ATLAS Insertable B-Layer Technical Design Report*,
ATLAS-TDR-19; CERN-LHCC-2010-013, 2010,
URL: https://cds.cern.ch/record/1291633 (cit. on p. 4).

[20] ATLAS Collaboration, *Performance of the ATLAS trigger system in 2015*,
Eur. Phys. J. C **77** (2017) 317, arXiv: 1611.09661 [hep-ex] (cit. on p. 4).

[21] ATLAS Collaboration, *ATLAS data quality operations and performance for 2015–2018 data-taking*,
JINST **15** (2020) P04003, arXiv: 1911.04632 [physics.ins-det] (cit. on p. 5).

[22] ATLAS Collaboration,
Luminosity determination in pp collisions at $\sqrt{s}$ = 13 TeV using the ATLAS detector at the LHC,
tech. rep. ATLAS-CONF-2019-021, CERN, 2019,
URL: http://cds.cern.ch/record/2677054 (cit. on p. 5).

[23] G. Avoni et al., *The new LUCID-2 detector for luminosity measurement and monitoring in ATLAS*,
JINST **13** (2018) P07017 (cit. on p. 5).

[24] ATLAS Collaboration, *Performance of the missing transverse momentum triggers for the ATLAS detector during Run-2 data taking*, JHEP **08** (2020) 080, arXiv: 2005.09554 [hep-ex]
(cit. on p. 5).

[25] ATLAS Collaboration, *Performance of the ATLAS muon triggers in Run 2*,
JINST **15** (2020) P09015, arXiv: 2004.13447 [physics.ins-det] (cit. on p. 5).

[26] ATLAS Collaboration, *Performance of electron and photon triggers in ATLAS during LHC Run 2*,
Eur. Phys. J. C **80** (2020) 47, arXiv: 1909.00761 [hep-ex] (cit. on p. 5).

[27] F. E. Paige, S. D. Protopopescu, H. Baer and X. Tata,
ISAJET 7.69: A Monte Carlo Event Generator for pp, $\bar{p}p$, and e^+e^- Reactions, (2003),
arXiv: hep-ph/0312045 [hep-ph] (cit. on p. 5).

[28] J. Alwall et al., *The automated computation of tree-level and next-to-leading order differential cross sections, and their matching to parton shower simulations*, JHEP **07** (2014) 079,
arXiv: 1405.0301 [hep-ph] (cit. on p. 5).

[29] T. Sjostrand, S. Mrenna and P. Z. Skands, *A Brief Introduction to PYTHIA 8.1*,
Comput. Phys. Commun. **178** (2008) 852, arXiv: 0710.3820 [hep-ph] (cit. on p. 5).

[30] D. J. Lange, *The EvtGen particle decay simulation package*, Nucl. Instrum. Meth. A **462** (2001) 152
(cit. on p. 5).

[31] L. Lonnblad and S. Prestel, *Matching Tree-Level Matrix Elements with Interleaved Showers*,
JHEP **03** (2012) 019, arXiv: 1109.4829 [hep-ph] (cit. on p. 5).

[32] ATLAS Collaboration, *ATLAS Pythia 8 tunes to 7 TeV data*, ATL-PHYS-PUB-2014-021, 2014,
URL: https://cds.cern.ch/record/1966419 (cit. on p. 5).

[33] S. Agostinelli et al., *GEANT4: A simulation toolkit*, Nucl. Instrum. Meth. A **506** (2003) 250
(cit. on p. 5).

[34] ATLAS Collaboration, *The ATLAS Simulation Infrastructure*, Eur. Phys. J. C **70** (2010) 823,
arXiv: 1005.4568 [physics.ins-det] (cit. on p. 5).

[35] S. Thomas and J. D. Wells, *Phenomenology of Massive Vectorlike Doublet Leptons*,
Phys. Rev. Lett. **81** (1 1998) 34,
URL: https://link.aps.org/doi/10.1103/PhysRevLett.81.34 (cit. on p. 5).

[36] W. Beenakker, R. Hopker, M. Spira and P. M. Zerwas,
Squark and gluino production at hadron colliders, Nucl. Phys. B **492** (1997) 51,
arXiv: hep-ph/9610490 (cit. on p. 5).

[37] ATLAS Collaboration, *Electron and photon performance measurements with the ATLAS detector using the 2015–2017 LHC proton–proton collision data*, JINST **14** (2019) P12006,
arXiv: 1908.00005 [hep-ex] (cit. on p. 6).

[38] ATLAS Collaboration, *Electron reconstruction and identification in the ATLAS experiment using the 2015 and 2016 LHC proton-proton collision data at $\sqrt{s} = 13$ TeV*, Eur. Phys. J. C **79** (2019) 639, arXiv: 1902.04655 [physics.ins-det] (cit. on p. 6).

[39] ATLAS Collaboration, *Muon reconstruction and identification efficiency in ATLAS using the full Run 2 pp collision data set at $\sqrt{s} = 13$ TeV*, (2020), arXiv: 2012.00578 [hep-ex] (cit. on p. 6).

[40] ATLAS Collaboration,
Topological cell clustering in the ATLAS calorimeters and its performance in LHC Run 1,
Eur. Phys. J. C **77** (2017) 490, arXiv: 1603.02934 [hep-ex] (cit. on p. 6).

[41] M. Cacciari, G. P. Salam and G. Soyez, *The anti-k_t jet clustering algorithm*, JHEP **04** (2008) 063, arXiv: 0802.1189 [hep-ph] (cit. on p. 6).

[42] M. Cacciari, G. P. Salam and G. Soyez, *FastJet User Manual*, Eur. Phys. J. **C72** (2012) 1896, arXiv: 1111.6097 [hep-ph] (cit. on p. 6).

[43] ATLAS Collaboration, *Jet energy scale and resolution measured in proton–proton collisions at $\sqrt{s} = 13$ TeV with the ATLAS detector*, (2020), arXiv: 2007.02645 [hep-ex] (cit. on pp. 6, 20).

[44] ATLAS Collaboration, *Performance of pile-up mitigation techniques for jets in pp collisions at $\sqrt{s} = 8$ TeV using the ATLAS detector*, Eur. Phys. J. C **76** (2016) 581,
arXiv: 1510.03823 [hep-ex] (cit. on p. 6).

[45] ATLAS Collaboration, *Performance of missing transverse momentum reconstruction with the ATLAS detector using proton–proton collisions at $\sqrt{s} = 13$ TeV*, Eur. Phys. J. C **78** (2018) 903,
arXiv: 1802.08168 [hep-ex] (cit. on pp. 6, 20).

[46] ATLAS Collaboration,
E_T^{miss} performance in the ATLAS detector using 2015–2016 LHC pp collisions,
ATLAS-CONF-2018-023, 2018, URL: https://cds.cern.ch/record/2625233 (cit. on p. 6).

[47] ATLAS Collaboration, *The Expected Performance of the ATLAS Inner Detector*,
tech. rep. ATL-PHYS-PUB-2009-002. ATL-COM-PHYS-2008-105, CERN, 2008,
URL: https://cds.cern.ch/record/1118445 (cit. on p. 6).

[48] ATLAS Collaboration,
Track Reconstruction Performance of the ATLAS Inner Detector at $\sqrt{s} = 13$ TeV,
ATL-PHYS-PUB-2015-018, 2015, URL: https://cds.cern.ch/record/2037683 (cit. on p. 6).

[49] M. Oreglia, 'A Study of the Reactions $\psi' \to \gamma\gamma\psi$', MA thesis, 1980 (cit. on p. 15).

[50] T. Skwarnicki,
'A study of the radiative CASCADE transitions between the Upsilon-Prime and Upsilon resonances',
PhD thesis: Cracow, INP, 1986 (cit. on p. 15).

[51] F. a. James, *MINUIT: Function Minimization and Error Analysis Reference Manual*,
(1998), CERN Program Library Long Writeups, URL: https://cds.cern.ch/record/2296388
(cit. on p. 18).

[52] W. Verkerke and D. P. Kirkby, *The RooFit toolkit for data modeling*,
eConf **C0303241** (2003) MOLT007, ed. by L. Lyons and M. Karagoz, arXiv: physics/0306116
(cit. on p. 18).

[53] J. Pumplin et al.,
New Generation of Parton Distributions with Uncertainties from Global QCD Analysis,
Journal of High Energy Physics **2002** (2002) 012, ISSN: 1029-8479,
URL: http://dx.doi.org/10.1088/1126-6708/2002/07/012 (cit. on p. 20).

[54] A. D. Martin, W. J. Stirling, R. S. Thorne and G. Watt, *Parton distributions for the LHC*, The European Physical Journal C **63** (2009) 189, ISSN: 1434-6052, URL: http://dx.doi.org/10.1140/epjc/s10052-009-1072-5 (cit. on p. 20).

[55] A. L. Read, *Presentation of search results: the CLs technique*, Journal of Physics G: Nuclear and Particle Physics **28** (2002) 2693, URL: https://doi.org/10.1088/0954-3899/28/10/313 (cit. on p. 21).